



universität
wien

DIPLOMARBEIT

Titel der Diplomarbeit

Monitoring of structural changes of the Gradenbach landslide using
signal correlations of near earthquake data

Verfasserin

Angela Isabella Domenig

angestrebter akademischer Grad

Magistra der Naturwissenschaften (Mag.rer.nat.)

Wien, 2013

Studienkennzahl:

A 416

Studienrichtung:

Diplomstudium Geophysik

Betreuer:

Em.O.Univ.Prof. Dipl.-Ing. Dr.phil. Ewald Brückl

Acknowledgments

Mein Dank gilt:

Prof. Ewald Brückl,
für die Übernahme des Diplomarbeitsthemas und für seine Geduld

Mag. Stefan Mertl,
für seinen Support in Sachen Programmieren und für sein offenes Ohr

Dr. Werner Chwatal,
für seinen Support in Sachen ProMAX

Walter Loderer,
für den technischen Support

meinen Eltern,
für den finanziellen Support und für ihr tiefes Verständnis

meinen Geschwistern,
für den seelischen Support und für ihre ehrliche Kritik

meinen StudienkollegInnen Martin, Franziska und Patrick,
für eine wunderbare Studienzeit!

ZUSAMMENFASSUNG

Massenbewegungen oder Hangrutschungen sind komplexe Prozesse, die naturgemäß in der geologischen Entwicklung von Bergregionen vorkommen. Oft werden sie mit wirtschaftlichen und sozialen Katastrophen in Verbindung gebracht, aber ihre Mechanismen und auslösenden Faktoren sind mannigfaltig und mitunter unbekannt. Auf der für diese Arbeit relevanten Gradenbach (GB) Massenbewegung, wurden bereits 1969 erste geotechnische und geodätische Untersuchungen durchgeführt, nachdem sie in den Jahren 1965 und 1966 beschleunigte, Schuttströme auslöste und das Dorf Putschall in Kärnten, Österreich zerstörte. Die Verwendung von Monitoring Netzwerken, bestehend aus mehreren über das Untersuchungsgebiet verteilten Seismometern, hat im Bereich der Seismik zu einer Vielzahl neuer Möglichkeiten geführt, Hangrutschungen permanent zu beobachten und zu analysieren.

In den an den Stationen aufgezeichneten Signalen finden sich neben Signalen, die von der Massenbewegung selbst ausgelöst werden, auch Signale von Erdbeben aus aller Welt. Diese Arbeit versucht herauszufinden, ob und welche Informationen über die strukturelle Beschaffenheit der Massenbewegung Gradenbach gewonnen werden können, wenn Signal Korrelationen durchgeführt und geeignete Reduktionsverfahren auf diese Erdbebendaten angewendet werden. Der Vergleich von Laufzeitdifferenzen von Wellen aus drei verschiedenen Richtungen über einen Zeitraum von zwei Jahren erlaubt möglicherweise eine Aussage über die physikalischen Eigenschaften der Massenbewegung selbst oder deren strukturellen Änderungen mit der Zeit.

Nachdem der Einfluss der unterschiedlich aufzeichnenden Seismometer rückgängig gemacht wurde (inverse filtering), werden zur Bestimmung der Laufzeiten Signal Korrelationen berechnet und anschließend die Korrelationsmaxima gepickt. Als Referenzsignal dient ein zuvor aus den Aufzeichnungen von GB03 ausgeschnittener Signalteil, der den Ersteinsatz enthält. Um Signale aus verschiedenen Richtungen und Distanzen miteinander vergleichen zu können werden folgende Reduktionen durchgeführt: eine Richtungsreduktion auf Basis einer orthogonalen Projektion um den Einfluss der Richtung rückgängig zu machen, eine Moho-dip Reduktion basierend auf der Änderung der Scheingeschwindigkeiten für geneigte Schichten um den Einfluss der Neigung der Mohorovičić Diskontinuität rückgängig zu machen und eine Höhen Reduktion um die Höhendifferenzen der einzelnen Stationen zu beachten. Die Endresultate zeigen, dass beinahe alle untersuchten Signale Station GB03 in der Mitte

der Massenbewegung, als Letzte erreichen. Zwar ist die Auflockerung des Gesteins an dieser Stelle groß (was zu Verzögerungen dieser Art führen könnte), doch reicht auf Grund der großen Picking-Fehler und der vereinfachten Annahmen für das Untergrundmodell die Genauigkeit der Resultate nicht aus, um eindeutige Schlüsse über die Struktur des Hanges oder die zeitlich strukturellen Veränderungen ziehen zu können.

ABSTRACT

Landslides are complex processes that occur naturally in the geological evolution of mountain areas. They often cause economical and social disasters but their mechanisms and triggering factors are various and sometimes unknown. At the Gradenbach (GB) landslide, pertinent to this study, first geotechnical and geodetic measurements were started in 1969, after the mass-movement accelerated in 1965 and 1966, triggering catastrophic debris flows and devastating the village of Putschall, Carinthia, Austria. Within the field of seismic applications, the usage of seismic monitoring networks, consisting of multiple seismometers spread over the moving rock mass, was leading to a variety of new possibilities to observe and analyse landslides permanently.

Besides signals coming from the movement itself, also earthquake signals occurring all over the world can be found within the individual monitoring stations' recordings. The goal of this thesis is to find out if and what kind of information about the structural properties of the Gradenbach landslide can be received, by carrying out signal correlations and applying the appropriate reduction techniques to these earthquake signals. In order to get an idea of the physical properties of the mass-movement itself or even structural changes with time, travel time differences of waves coming from three different directions over a period of two years are investigated.

Signal correlations are carried out, using parts of the recording from station GB03 including the first break as reference signal to pick the travel times. Furthermore, to be able to compare the signals with each other three reductions are applied after reversing the influence of the (different) seismometers on the signals recorded (inverse filtering): a directivity reduction on the basis of an orthogonal projection to reverse the influence of direction, a Moho-dip reduction based on the change of apparent velocities for dipping layers to reverse the influence of the incline of the Mohorovičić discontinuity and a height reduction to regard the stations' height differences as well. The final results show, that almost all waves arrive last at station GB03 in the middle of the landslide. There the loosening of the rock mass is large (which could lead to these kind of travel time delays) but due to errors coming with time picking and simplified assumptions for modelling the subsurface, the accuracy of the results is insufficient to draw accurate conclusions on the structure of the landslide or even structural changes with time.

Table of contents

1. Introduction.....	1
1.1. Landslides.....	3
1.1.1. Causes of landslides.....	3
1.1.2. Classification of landslides.....	3
1.1.3. Deep-seated gravitational creep.....	4
2. Investigation area.....	6
2.1. Previous mass-movements and investigations.....	9
2.2. Structure and physical properties of the moving rock mass.....	10
2.2.1. Evidence from boreholes.....	10
2.2.2. Evidence from seismic investigations.....	11
2.3. Monitoring network.....	13
3. The data and its processing.....	14
3.1. Receiving the raw data.....	15
3.2. Data selection and preparation.....	16
3.2.0. Excursion: Seismon - the software used.....	16
3.2.1. Importing location, time and magnitude of seismic events	16
3.2.2. Imposing restrictions on the seismic events.....	17
3.2.2.1. The epi-distance.....	17
3.2.2.2. The magnitude.....	17
3.2.2.3. The direction.....	17
3.2.2.4. The visibility.....	19
3.2.2.5. The date.....	20
3.2.3. The dataset.....	21
3.2.4. Inverse filtering.....	23
3.2.5. Data export.....	29
3.3. Time picking using signal correlations.....	30
3.3.1. Data import.....	30
3.3.2. Signal Correlation	33
3.4. Calculating theoretical travel time differences.....	35
3.4.1. Receiving the ray parameter p using the TauP toolkit.....	35
3.4.2. Applied reductions.....	36

3.4.2.1. Moho-dip reduction	36
3.4.2.2. Directivity reduction.....	38
3.4.2.3. Height reduction.....	43
4. Results.....	45
5. Conclusion.....	48
5.1. Errors.....	49
5.1.1. Time picking.....	49
5.1.2. Applied reductions.....	49
5.1.3. Statistics.....	50
5.2. Outlook.....	51
6. Theoretical and mathematical background.....	52
6.1. Transformation of functions - integral transformations.....	53
6.1.1. Fourier transform.....	53
6.1.2. LaPlace transform.....	54
6.1.3. z transform.....	54
6.2. Linear time invariant systems (LTI systems).....	56
6.2.1. The frequency response function and the Fourier transform.....	57
6.2.2. The transfer function and the LaPlace transform.....	60
6.2.3. The impulse response function.....	60
6.2.4. Bilinear transform	61
6.3. The seismometer – an example for a LTI.....	63
6.3.1. Frequency response function of a seismometer.....	64
6.3.2. Transfer function of a seismometer.....	65
6.4. Correlation.....	66
6.4.1. Noise reduction.....	66
6.4.2. Time delay estimation.....	67
6.5. Ray theory.....	68
6.5.1. Ray geometry and the raypath equation.....	69
6.5.1.1. The travel time equation: the where and the when.....	71
6.5.2. Travel times in a layered earth.....	72
6.5.2.1. Apparent velocity and horizontal slowness.....	72
6.5.2.2. Travel time equation for a layered earth.....	73
6.5.2.3. The crossover distance	73
6.5.2.4. Apparent velocities for dipping layers.....	74

Bibliography.....75
List of figures.....77

1. Introduction

Landslides, mass-movements or moving rock masses are complex processes that occur naturally in the geological evolution of mountain areas. They are often associated with economical and social disasters but their mechanisms and triggering factors are various and sometimes unknown. Thus, it should be of particular importance to improve the understanding of how they work, what is causing them, and when.

After the mass-movement pertinent to this study, the Gradenbach (GB) landslide, accelerated in 1965 and 1966, triggering catastrophic debris flows and devastating the village of Putschall, first geodetic and geotechnical measurements were started in 1969.

Within the field of seismic applications, the development of affordable, robust instruments, compact data storage and easy data transmission was leading to a variety of new possibilities to analyse landslides and their movements. To gather information about landslides, the usage of so called seismic monitoring networks still gains in importance. These networks consist of multiple seismometers spread over the moving rock mass, permanently recording different types of signals.

Signals of interest may come from the movement itself but also signals coming from earthquakes all over the world can be found within the recordings of the individual monitoring stations. The main aim of this study is to find out if and what kind of information can be dragged out by applying the appropriate processing to these earthquake signals.

The comparison of travel times of waves coming from an earthquake might be a way to get an idea of the physical properties of the landslide itself or even structural changes with time. One big advantage is the passivity of this method since no additional sources have to be installed.

To start with, when wanting to compare travel times of signals being recorded by different seismometers (as it is the case in this study), it is necessary to reverse the influence of the instrument on the recorded signal first. Therefore a filter consisting of the inverse transfer function of the particular seismometer in combination with a bandpass has been applied.

Afterwards, to receive - early or delayed - arrival times relatively to a reference station, signal correlation using ProMAX has been carried out. The designated reference

signal is part of the signal recorded on reference station GB03, including the first break (P or Pn). The maxima of the cross correlations represent the point of time when maximum correlation was achieved, which means that picking the maximum of the signal correlation function returns the value of time when the designated signal appears within the other trace.

For a comparison of travel time differences of waves coming from different directions, it is necessary to reverse the influence of direction on the recorded signal. Assuming that wave fronts reach the stations as wave fronts of a plane wave, the distances the waves have to cover between the individual stations depend on the direction of the incoming wave fronts relatively to reference station GB03. Thus, a directivity reduction on the basis of an orthogonal projection has been used.

In case of a Pn wave as first arrival the incline of the Mohorovičić discontinuity has been taken into account by applying a Moho-dip reduction based on the change of apparent velocities for dipping layers.

Furthermore to regard the stations' height differences, the data has been height reduced as well.

Three clusters of a total of 43 individual events occurring in three different directions and distances from the landslide over a period of two years have been investigated. Due to mechanical limitations resulting from the usage of mainly 4.5 Hz seismometers only near earthquakes with an epicentral distance smaller than 1000 km have been taken into account.

1.1. Landslides

There is no unified definition for the term landslide. Sometimes it is used in a broad sense meaning downward and outward mass-movements in general, other times it is used for a certain kind of mass-movement only.

Generally the movement involves the development of a sliding surface. Hence the displaced material can be sharply distinguished from the unmoving area. Landslides are unavoidable discontinuous processes that occur in the natural geological evolution of mountain areas. Periods of limited activity can be followed by calamitous events that have often been associated with economical and social disasters. To prevent damage it would be necessary to predict not only the volume of a potential landslide, but also when it will occur. Since the triggering factors are various and sometimes unknown, especially the moment when a mass actually starts its movement is very hard to predict. (Marui 1988: 1-6, Brückl et al. 2006a: 149-150)

1.1.1. Causes of landslides

In most cases a number of causes contribute towards movement but still the common force tending to generate movement is gravity. The mass in a slope is subjected to gravity which is usually balanced by the shear strength of the material concerned, making the slope stable. There are numerous elements which influence slope stability but altogether, landslides occur because the forces creating movement exceed those resisting it. (Bell 1998: 84-86)

"If along a potential sliding surface in the slope shear stress from any source (such as groundwater, earthquakes or constructions) exceeds the shear strength of the soil along the surface, shear failure and movement occur. The loss of balance arises with either increased shear stress or decreased shear strength, or both." (Marui 1988: 6)

1.1.2. Classification of landslides

Due to the complexity of slope movements there are many classifications of landslides but the one most widely used is that of Varnes (1978). He was introducing two main criteria for classifying landslides: the type of movement on the one hand and the type of material involved on the other. (Bell 1998: 88)

TYPE OF MOVEMENT		TYPE OF MATERIAL	
		BEDROCK	ENGINEERING SOILS
			Predominantly coarse Predominantly fine
FALLS		Rock fall	Debris fall Earth fall
TOPPLES		Rock topple	Debris topple Earth topple
SLIDES	ROTATIONAL	Rock slide	Debris slide Earth slide
	TRANSLATIONAL		
LATERAL SPREADS		Rock spread	Debris spread Earth spread
FLOWS		Rock flow (deep creep)	Debris flow Earth flow (soil creep)
COMPLEX		Combination of two or more principal types of movement	

Figure 1.1 abbreviated version of Varnes' classification of slope movements (1978)

(Source: <http://pubs.usgs.gov/fs/2004/3072/pdf/fs2004-3072.pdf> [2013-02-27])

Expressed in simplified terms the five main types of movements are: falls, topples, slides, spreads and flows. This study takes a closer look at a phenomenon that has been frequently observed on Alpine slopes and which is called deep-seated gravitational creep, rock flow or sagging of rock masses.

1.1.3. Deep-seated gravitational creep

"Deep-seated gravitational creep in rocks, rock flow or sackung is a special category of mass-movement, in which long-lasting-small-scale movements prevail. The prime causes of these mass-movements in the Alpine area seem to have been glacial retreat at $\sim 15\,000$ a B.P. Many sackung stabilize and some undergo the transition to rapid sliding." (Brückl et al. 2005: 155)

Crystalline rocks of different metamorphic grades frequently undergo deep-seated gravitational creep. The rock material forming sagging slopes is best described as brittle rock since it has not been altered significantly by weathering. The typical thickness of slopes involved is 100 m and the volume of the creeping rock mass is about 10^8 m^3 or even larger. Surface velocities reach from millimetres to some metres per year and vary significantly with time. Phases of relatively high velocities alternate with periods of lower activity. The movements are known to be influenced by precipitation and

groundwater level variations but modelling these effects has been rather difficult since it is not so simple as it is for shallow mass-movements in soil. (Brückl et al. 2006b: 255)

Especially through deep-seated mass-movements, deformations, thus fabric changes of the original range formation occur. This leads to areas of effective partial mobility within a potential consistently moving rock mass. Hereby structural geological units form that are hydrogeologically operative as well. (Weidner et al. 2011: 23)

2. Investigation area

The Gradenbach landslide, a deep-seated mass-movement, is located in the crystalline rocks of Schober mountain range, south of the central Eastern Alps at the intersection of the Graden and the Möll valleys near Döllach, Carinthia, Austria.

From a tectonical and geological point of view the area around the landslide can be divided into three different zones: the Penninic Zone (Penninic Tauern-window), the Matrei Zone and the Austroalpine Zone, with the actual landslide being situated in the Matrei Zone only. (Brückl et al. 2006: 255-256)

The active deformation zone is located close to the village of Putschall, at the southeast side of the Eggerwiesenkopf.

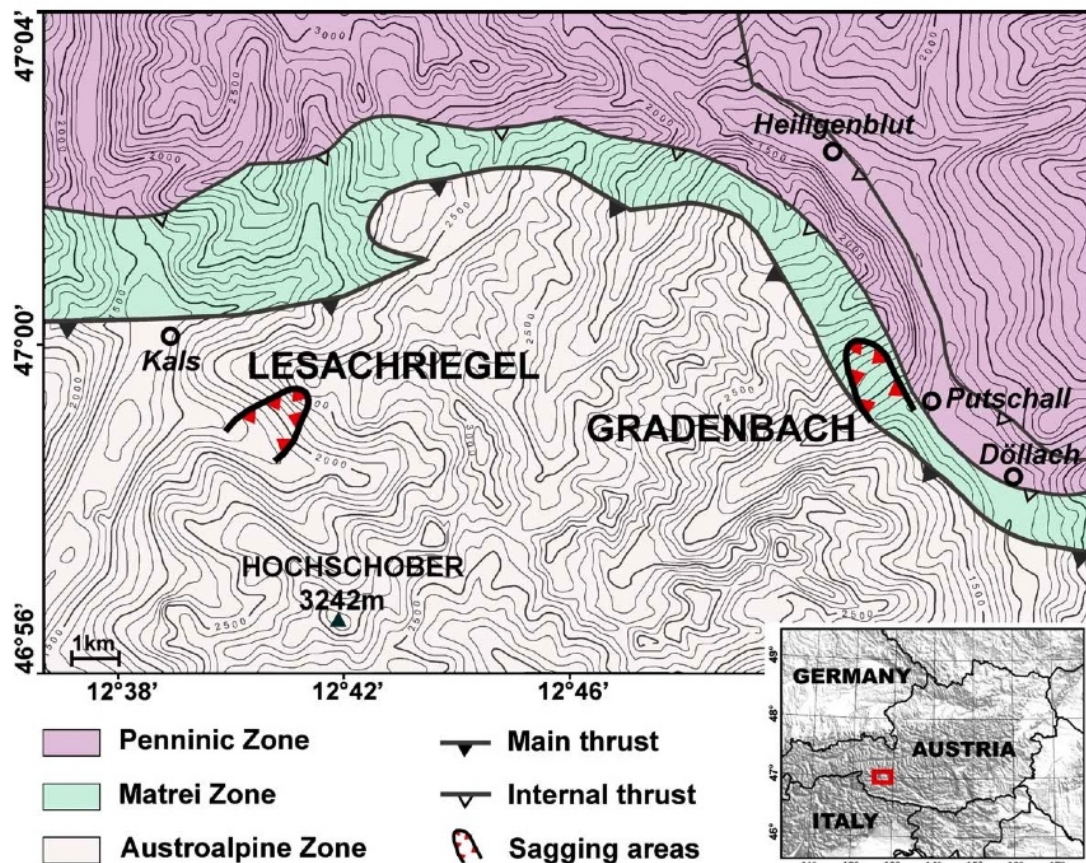


Figure 2.1 tectonic map and location of the Gradenbach deep-seated mass-movement

(Source: Brückl et al. 2006b: 255)

With width ranging between 600 and 1000 m, and an extent of approximately 1000 m in height, from the clearly developed head scarp at 2270 m down to the slide toe, at a height between 1100 and 1270 m, the landslide involves an area of about 1.7 km². (Brückl et al. 2006a: 150)

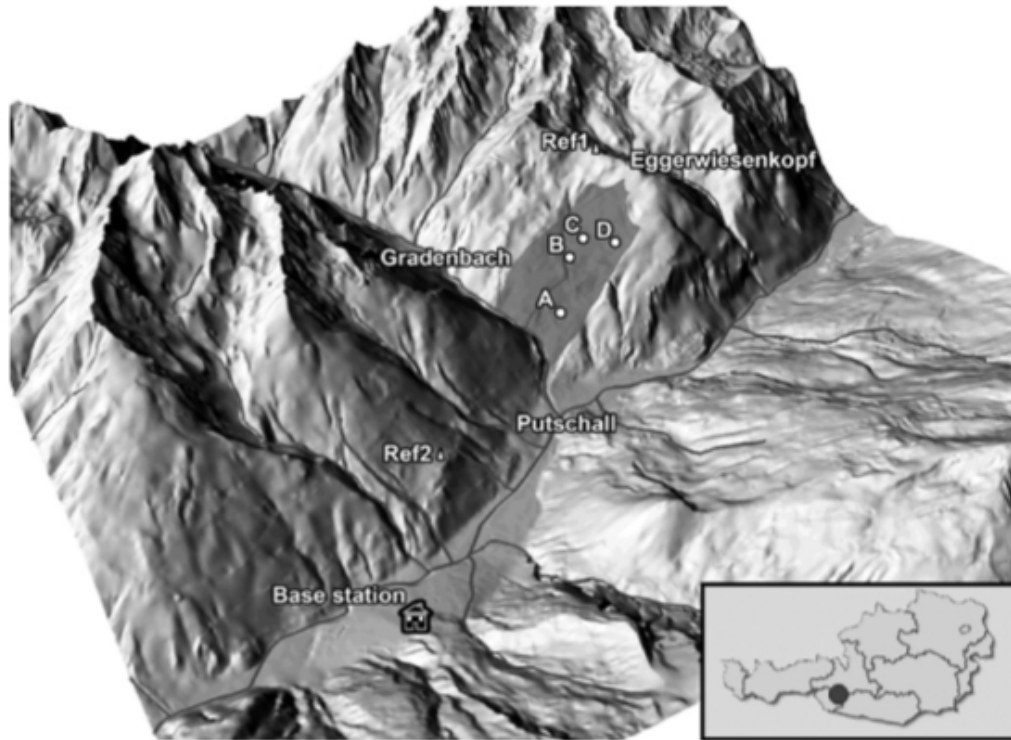


Figure 2.2 topography of the Gradenbach landslide area: all GPS stations of the monitoring network are shown; for scale estimation: the horizontal distance between Ref2 and A is 2600 m

(Source: Brückl et al. 2006 a: 150)

Rocks - types and distribution

In contrast to the middle and western parts of the moving mass that mainly consist of carbonate-free metasediments of the Mafrei Zone (chlorite-phyllites, quartzites and sericite-phyllites), the eastern part is dominated by darkgrey lime-mica-phyllites. (Weidner et al. 2011: 22)

Rocks of the upper Glockner-nappe system make up the largest part of the eastern boundary of the landslide (carbonate-micaschists). Rocks of the Petzeck-Rottenkogel complex, mainly consisting of garnet-micaschists and paragneisses, make up the largest part of the western nappe-boundary to the east alpine Schober crystalline. Occasionally

serpentine-steatite, dolostone-breccia and yellowish greywacke outliers that disintegrate to sandy grus can be found. (Weidner et al. 2011: 22)

With a thickness up to 5 m the solid rocks are partly covered with rockfall material, moraines and fluvioglacial sediments. The weathering cover, with a thickness of less than 1 m, is relatively small. (Weidner et al. 2011: 22)

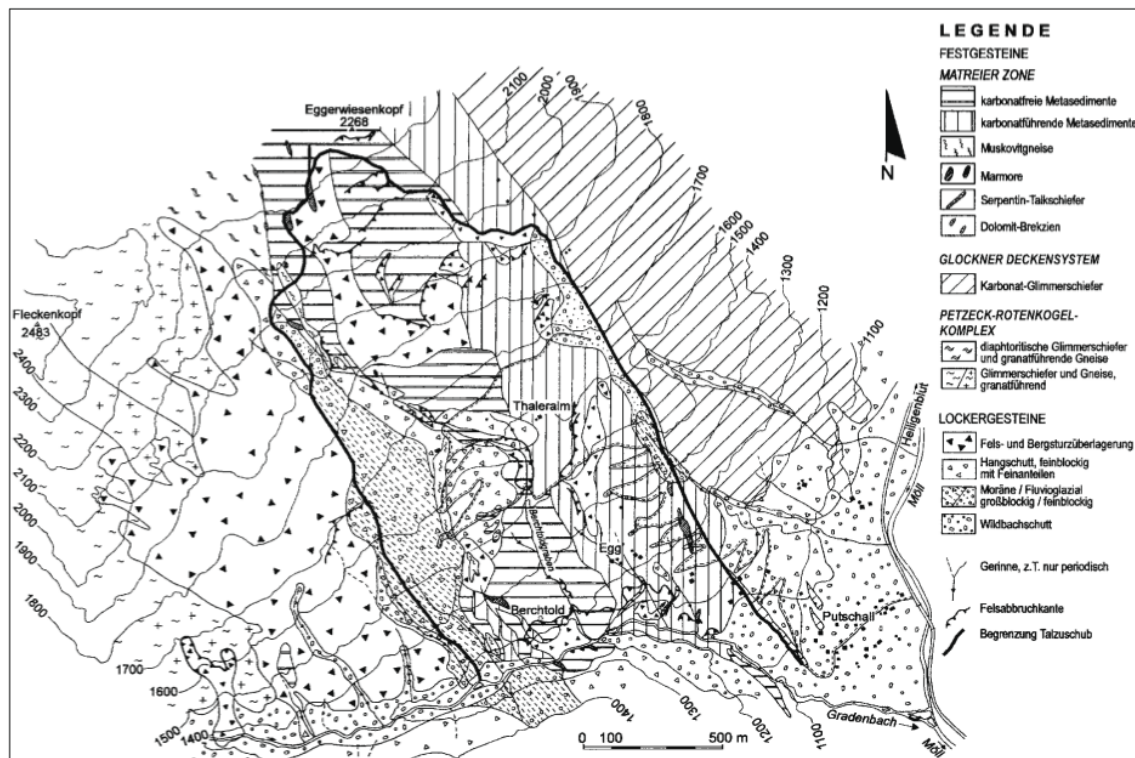


Figure 2.3 geologic-geotechnical map of the Gradenbach landslide

(Source: Weidner et al. 2011: 22)

2.1. Previous mass-movements and investigations

When examining old pictures of the investigation area the first evidence of sliding-motions of the Gradenbach landslide can be found in 1870 and between 1880 and 1885. By oral tradition, first movements of the SE-flank of the Eggerwiesenkopf occurred after a very snowy winter in the year 1917. (Weidner et al. 2011: 19)

The first control structures have been applied in the 1930s. Geodetic and geotechnical measurements were started in 1969 after the mass-movement accelerated in 1965 and 1966, triggering catastrophic debris flows and devastating the village of Putschall (fig. 2.4). (Weidner et al. 2011: 20)



Figure 2.4 devastated village of Putschall (1968)

(Source: Weidner et al. 2011: 20)

Geophysical models could already be submitted in the 1980s (Brückl, 1984) followed by papers in even more detail, including diverse geotechnical analysis since the late 1990s. (Weidner et al. 2011: 21)

GPS observations were started in 1999, revealing an average creep rate of 0.6 m/year between 1999 and 2003 at 4 stations distributed over the whole slope which - taking into account the larger displacements in 1965 and 1966 and also during the summer of 2001, with a creep rate of 0.2 m/month - is regarded as a quite reliable estimate for the last 50 years. (Brückl et al. 2006b: 258)

2.2. Structure and physical properties of the moving rock mass

The base as one of the most important structural elements of a moving rock mass may either be a transition zone or, as in this case, a significant discontinuity and may therefore be identified and later referred to as the basal (sliding) plane.

Information about the basal plane may be derived from the geological and rock mechanical interpretation of boreholes, or from e.g. seismic investigations. (Brückl et al. 2006b: 258)

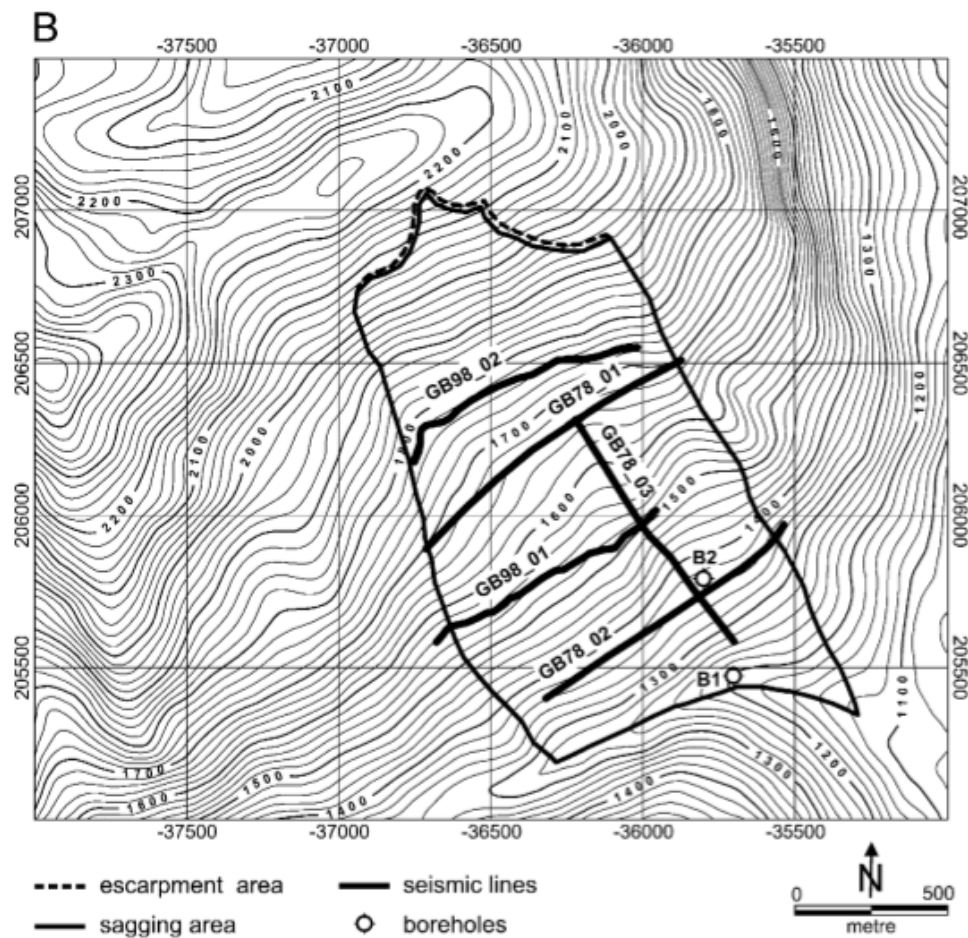


Figure 2.5 topography and location of seismic lines and boreholes

(Source: Brückl et al. 2006b: 256)

2.2.1. Evidence from boreholes

From the boreholes that have been drilled mainly for hydrogeological purposes, two give information about the basal plane:

One borehole (B1) is located in the valley where the sagging rock mass overthrusts moraines - at the so called toe area of the mass-movement. At a depth of 35 m compact and stable rock has been found. (Brückl et al. 2006b: 259)

The other borehole (B2) is located in the lower bulge of the sagging rock mass. Drilling was stopped at a depth of 132 m in a distinct shear zone and is therefore taken to be the minimum depth for the basal plane. (Brückl et al. 2006b: 259)

2.2.2. Evidence from seismic investigations

Older seismic refraction data from the years 1976 (one longitudinal line from the scarp down to the steep slope) and 1978 (one longitudinal and 3 transverse lines) already give clear evidence about the basal plane. (Brückl et al. 2006b: 259-260)

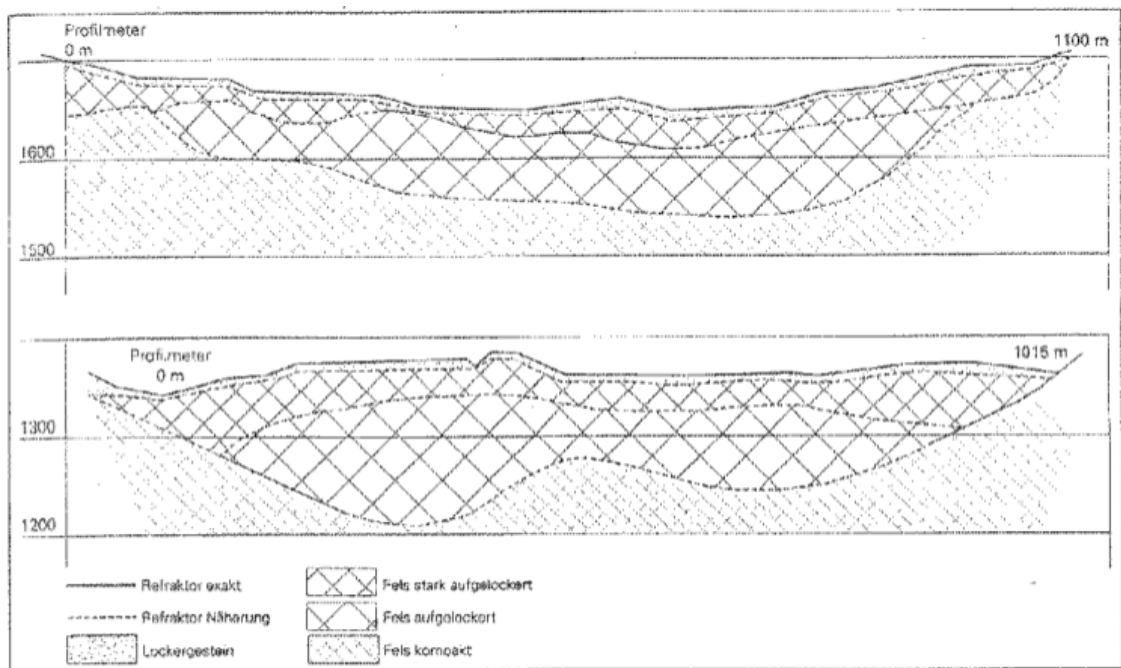


Figure 2.6 seismic cross sections of Gradenbach landslide
(above: GB78_01, below: GB78_02)

(Source: http://www.ktn.gv.at/9923_DE-Geologie_und_Bodenschutz-GB_DEEP_CREEPING_MASS_MOVEMENTS_.pdf [2013-02-27])

Further seismic investigations have been carried out in the summer of 1998 (2 transverse lines). The basal plane produced clear first arrivals of refracted P-waves at

offsets larger than 200-400 m. By application of the so called survey-sinking concept an accurate imaging of the discontinuity in the velocity field was done.

The average P-wave velocity of the compact rock below the basal plane is 4740 m/s. (Brückl et al. 2006: 260-261)

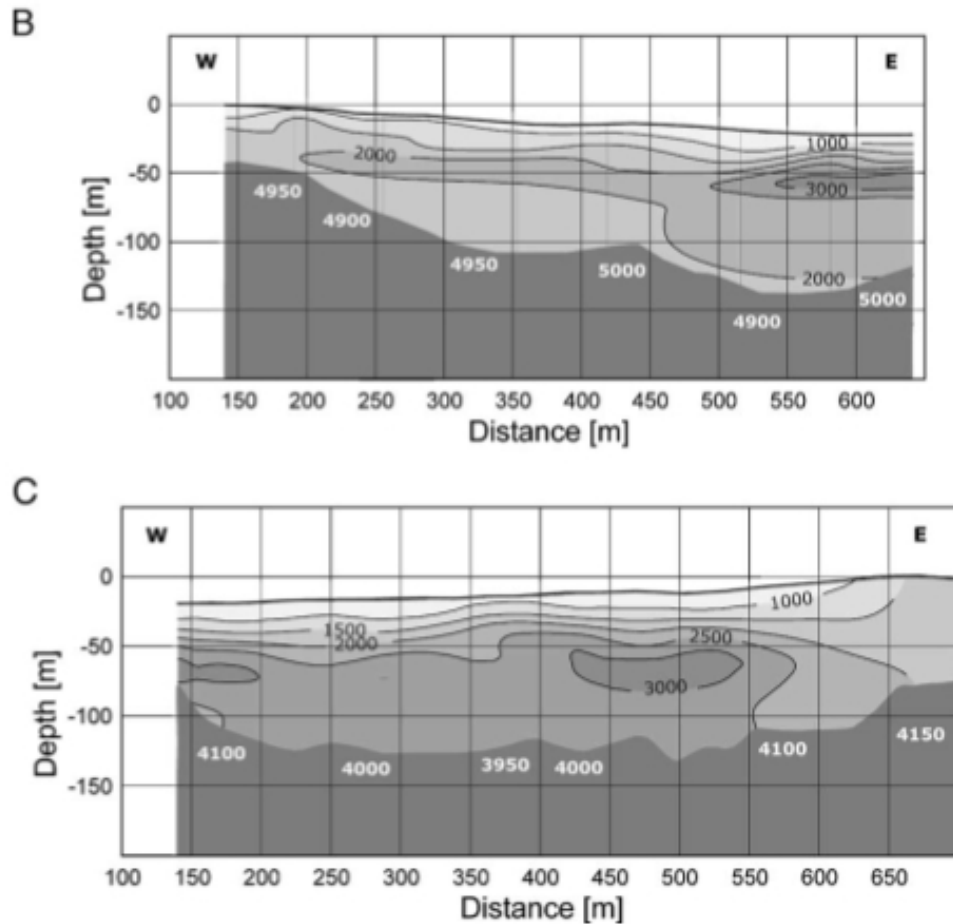


Figure 2.7 P-wave velocity models of the creeping rock mass and the stable rock base (B) GB98_01, (C) GB98_02

(Source: Brückl et al. 2006b: 259)

2.3. Monitoring network

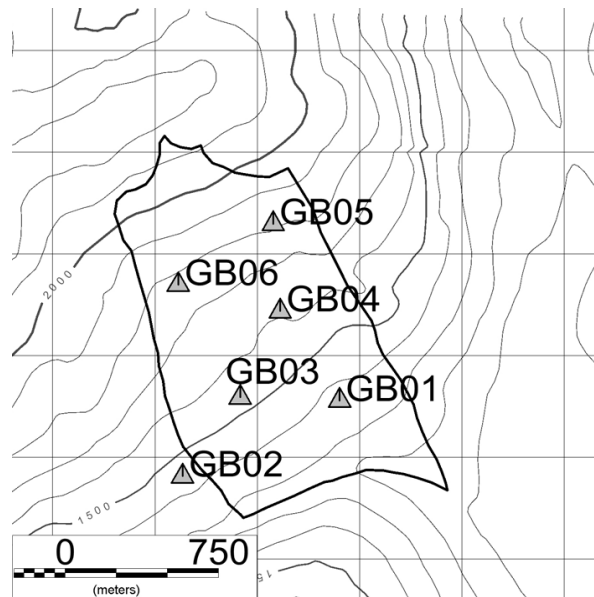


Figure 2.8 Gradenbach monitoring network

(Source: Mertl et al. 2008: 3)

Within the scope of the ISDR-20 project of the Vienna University of Technology, whose task is to integrate geodetic and geophysical monitoring into a uniform surveillance system for deep-seated mass-movements, six permanent seismic monitoring stations have been installed at Gradenbach since August 2006. The sensors are buried at a depth of 60 cm at least, the stations have solar power supply and a lightening protection. (Mertl et al. 2008: 1-3)

Station	Recorder	Sensor
GB01, GB02, GB03, GB05, GB06	Reftek 130-01	Geospace GS-11 D 4.5 Hz 3 components
GB04	Reftek 130-01	Geospace GS-1 SeisMonitor 1 Hz 3 components

Table 1.1 Seismic equipment used for monitoring

The data is recorded continuously with a sampling frequency of 200 Hz during summer and 100 Hz during winter to prevent data loss caused by data storage overflow.

3. The data and its processing

The first part of this chapter deals with the receiving of the raw data and the data selection and preparation. In order to decide which events are going to be used for further processing, some restrictions have to be imposed.

After the data selection is complete, the influence of the individual seismometer on the recorded data has to be reversed. Thus, a filter consisting of the inverse transfer function of a seismometer in combination with a bandpass has to be applied.

To receive travel time differences of waves reaching the monitoring stations relatively to each other, signal correlations have been carried out. Picking the maxima of the cross-correlation functions and subtracting the reference stations' time value from the other ones, will lead to an expression of early or delayed arrival times.

Furthermore, in order to be able to compare travel time differences of waves coming from different directions, and to regard the stations' height differences as well, a few reductions have to be applied.

3.1. Receiving the raw data

As mentioned before the data of six seismic stations over a period of almost two years has been taken into account. All stations excluding one (GB04) are 4.5 Hz seismometers, GB04 is a 1 Hz seismometer. This fact of course will not only have an influence on the recording but also on the processing of the signals later on.

The recording unit used is a Reftek 130-01 which incorporates a seismic recorder with a 24-bit delta sigma analog-to-digital converter. It has two input channel connectors (3 to 6 channels) for connection to any geophysical sensor available and can be equipped with one or two compact flash card storage media (disks). The data can be collected on site by swapping the compact flash cards.¹

Approximately every 3 months the data is collected but especially from November to March, when the stations are not safely accessible, the interval cannot be sustained and therefore data loss might occur. (Mertl et al. 2008: 3-4)



Figure 3.1 recording unit Reftek 130-01

(Source: <http://www.reftek.com/products/seismic-recorders-130-01.htm> [2013-02-27])

For further processing the raw data has been converted to the miniSeed format.²

1 For further information: <http://www.reftek.com/products/seismic-recorders-130-01.htm>
[last downloaded: 2013-02-27]

2 For further information: http://www.iris.edu/manuals/SEEDManual_V2.4.pdf
[last downloaded: 2013-02-27]

3.2. Data selection and preparation

3.2.0. Excursion: Seismon - the software used

Seismon is an open source software project written by Stefan Mertl to mainly facilitate the scientific work of smaller seismic research projects. It is written in Matlab using a MySQL database as storage space for the data and is quite similar to handle to other well known software for seismic processing. Seismon does not only take care about the import, the management and the display of seismic data but it also includes basic seismic processing algorithms such as e.g. frequency filtering, spectral analysis, time picking etc. Furthermore it has a flexible recorder and station geometry management and also the data visualization is flexible.³

3.2.1. Importing location, time and magnitude of seismic events

Besides importing miniSeed data, Seismon can also import data from earthquake bulletins received after sending an AutoDRM bulletin request.⁴

The request, in this case addressed to the Austrian Central Institution for Meteorology and Geodynamics (ZAMG), returns a list of coordinates of hypocentres, magnitudes, dates and times of events, occurring all over the world within the desired period of time (e.g. two years).

Just like the raw data from the investigation side, also the bulletin data is stored in the MySQL database and can easily be accessed through any function or program written in Matlab simply by connecting to the database and implying a MySQL query to retrieve the data needed for taking further action.

Mainly due to data quality reasons, not all of the events will be taken into account, so it is necessary to impose some restrictions and to classify them first in order to select the appropriate ones.

3 For further information: <http://www.stefanmertl.com/science/software/seismon/>
[last downloaded: 2013-02-27]

4 For further information: <http://www.iris.edu/manuals/autoDRM.htm> [last downloaded: 2013-02-27]

3.2.2. Imposing restrictions on the seismic events

3.2.2.1. The epi-distance

The further the waves have to travel from the hypocentre to the recording units, the lower the frequency content of the signal. Since preserving higher frequencies means preserving information and also because most of the receivers are 4.5 Hz seismometers, only earthquakes with an *epi-distance* $d \leq 1000$ km were taken into account.

Limitation no. 1: near earthquakes only

$d \leq 1000$ km

d... epi-distance

3.2.2.2. The magnitude

The second limitation regards the magnitude of the seismic events. Only events showing higher local magnitudes were used for further processing. In fig. 3.2 the different magnitudes are indicated by different colours.

Limitation no. 2: preference for events with higher local magnitudes

3.2.2.3. The direction

When comparing travel time differences throughout the year, it is necessary to make sure, that the waves reaching the stations come from the same or a similar direction at least. Events occurring within a particular direction from the landslide will be combined into one cluster of events.

To display both the epicentral distance and the direction of the propagating wave front in one plot, a polar plot with the GB stations in the centre of it has been used. To get the distances and the directions relatively to the GB stations Matlab has a function `distance(lat1,lon1,lat2,lon2)` that computes the distance(s) and the back azimuth(s) between given points along a great circle on the surface of a sphere by entering their coordinates.

In this case the coordinates are the stations' and epicentres' respectively. The locations of the epicentres relatively to the GB stations were plotted in a polar plane

where the radial distance from the origin of the plot is equivalent to the epicentral distances (in degrees) of the various events while the backazimuths represent the directions of the incoming wave fronts (fig. 3.2). Note: compared to the common conventions of a polar plane the polar angle is NOT the counter clockwise angle from the x-axis but the clockwise angle from the y-axis.

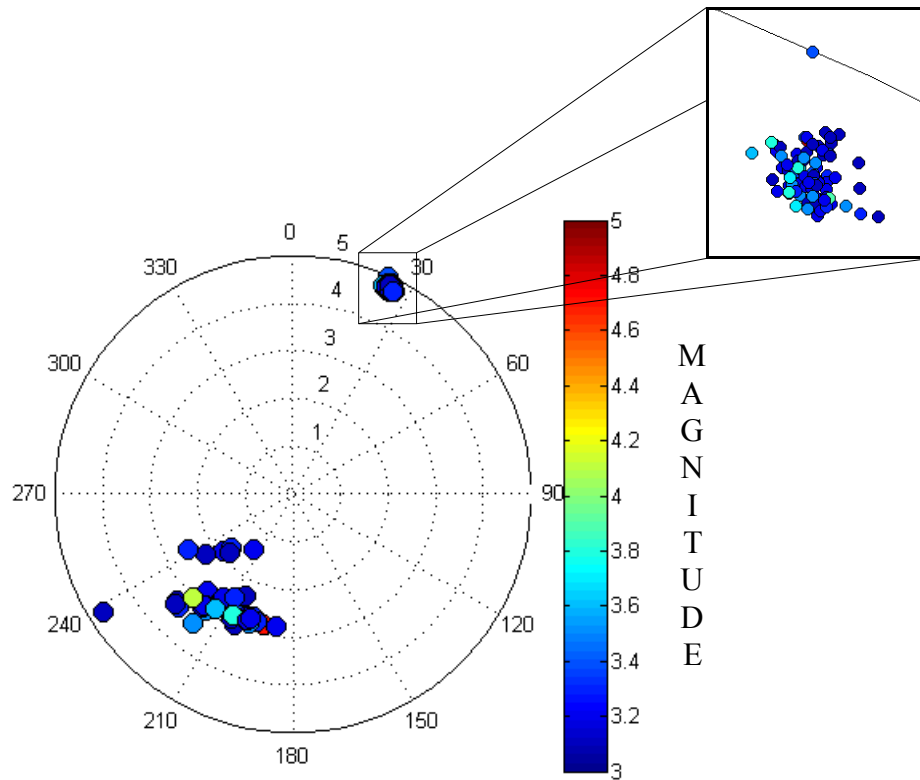


Figure 3.2 polar plot of "visible" near earthquakes; the radius is the epi-distance in degrees; for data selection purposes a function returns the information needed to find the events in the database when clicking on the individual marker; author: myself

Since the bulletin request returned hundreds of events occurring within an epicentral distance $d \leq 1000$ km and a time period of two years, it might be difficult to spot clusters of events and also to tell of how many events one cluster consists. Generating a histogram that shows from which direction most of the wave fronts come from is very helpful to get an idea where to look first (fig. 3.3).

Note: It might not seem too difficult to find clusters of events in fig. 3.2 but for reasons of simplification only "visible" earthquakes are being displayed (cf. chapter 3.2.2.4).

Knowing the direction where to find clusters of events one can take a closer look by zooming into the wished region of the polar plot (fig. 3.2). By clicking on the individual marker a function will return the parameters that are necessary to find the selected events in the database and to mark the time of their occurrence when displaying the GB stations' recordings .

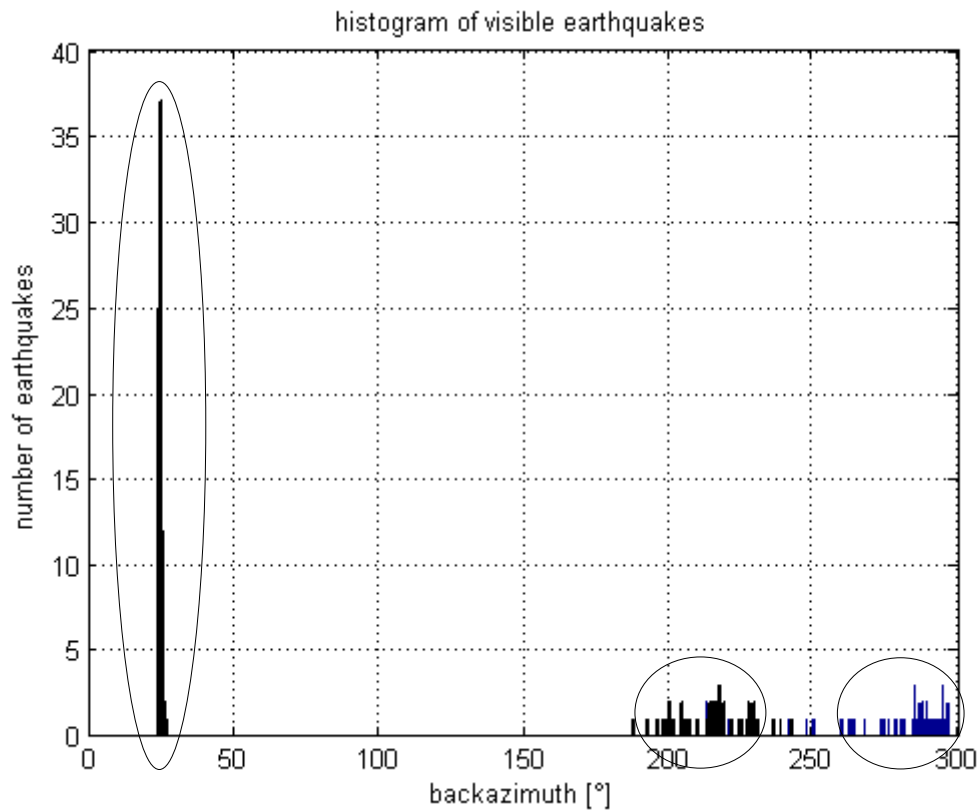


Figure 3.3 histogram of "visible" local earthquakes (blue) and near earthquakes (black) with different magnitudes; "local" means an epicentral distance smaller than 150 km; the x-axis indicates the direction of the occurring events relative to the GB monitoring stations; the circles mark the directions where to look for clusters of events in the polar plot (fig. 3.2)

Limitation no. 3: clusters of events only

3.2.2.4. The visibility

Mainly due to noise the earthquake signals can sometimes not be seen immediately thus, it is necessary to check whether the selected events as a result of the limitations above can at all be seen within the recordings of the monitoring stations or not. Seismon band-pass-filters and displays the recorded seismic data and marks the point of time where the selected events occurred (fig. 3.4). This enables the user to

classify the events into “visible” and “not visible” ones. Of particular interest are signals that have a high S/N-ratio and therefore a clear first arrival.

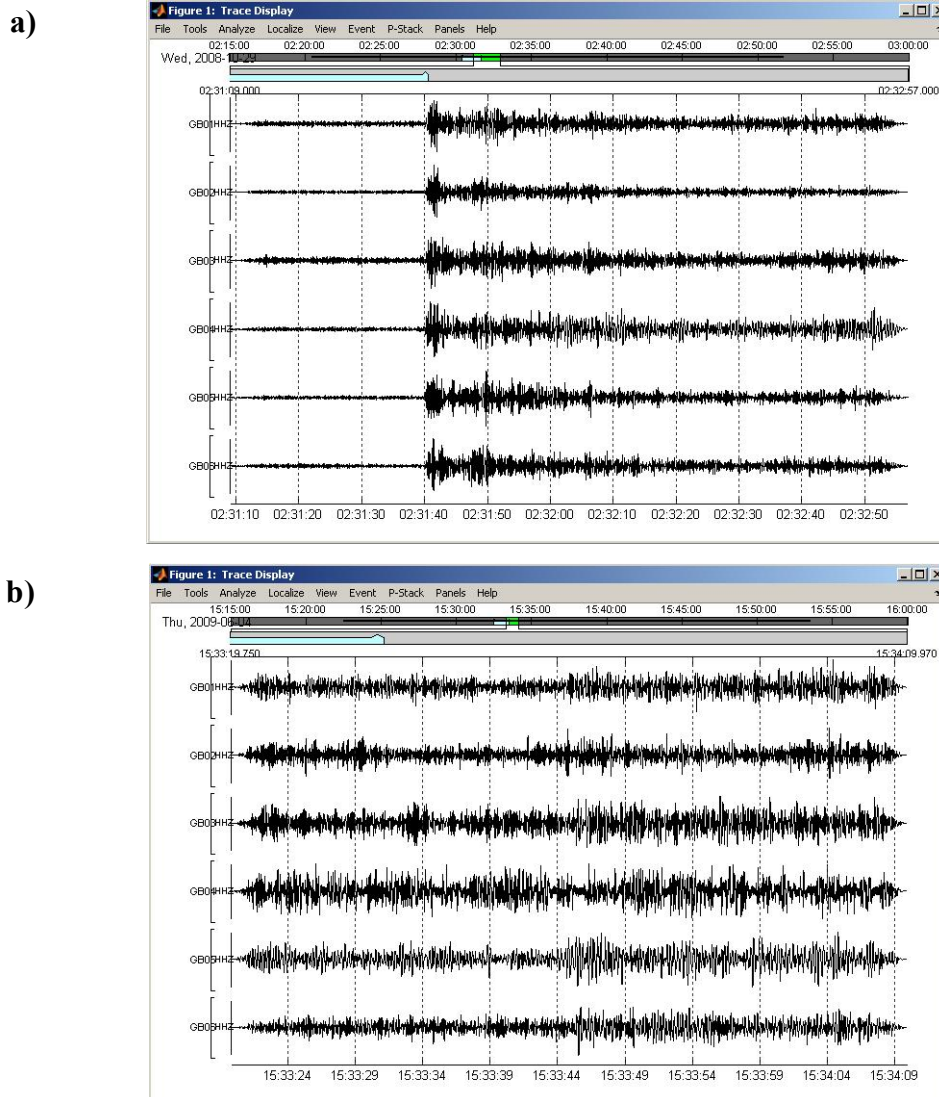


Figure 3.4 visible (a) and not visible (b) event filtered with a 4th order butterworth band-pass (lower cut-off: 2Hz, upper cut-off: 12 Hz);

3.2.2.5. The date

Besides the spatial distribution, the temporal distribution of data is of importance as well. The best case would be data from events evenly spread over the year (one to two per month), but since earthquakes do not occur that regularly and due to noise and data loss during winter this could not be achieved (fig. 3.6).

<p>Limitation no. 4: events evenly spread over the year</p>
--

3.2.3. The dataset

After imposing and applying the limitations above, a total of 43 events occurring within an epicentral distance $d \leq 1000$ km were chosen to be the final dataset used for further processing.

In order to "cover" a range of possible directions of arriving wave fronts of 360° , events occurring in three different directions from the stations have been taken into account. The three clusters of events were named after the countries where the incident wave fronts originally come from (fig. 3.5).

	name	no. of events	$\vartheta_{\text{mean}} [^\circ]$	m_L
1	POLAND	16	25	≥ 3
2	ITALY	21	210	≥ 2
3	AUSTRIA	6	280	≥ 1

Table 3.1 final dataset

ϑ_{mean} ... backazimuth
 m_L ... local magnitude

It has to be mentioned, that the data selection was iterative which means that e.g. after limiting the magnitudes the visibility was checked and if there were not enough visible events left for the designated period of time, the selection was extended to events showing lower local magnitudes as well etc.. However, table 3.1 indicates the lowest local magnitude of events used for further processing.

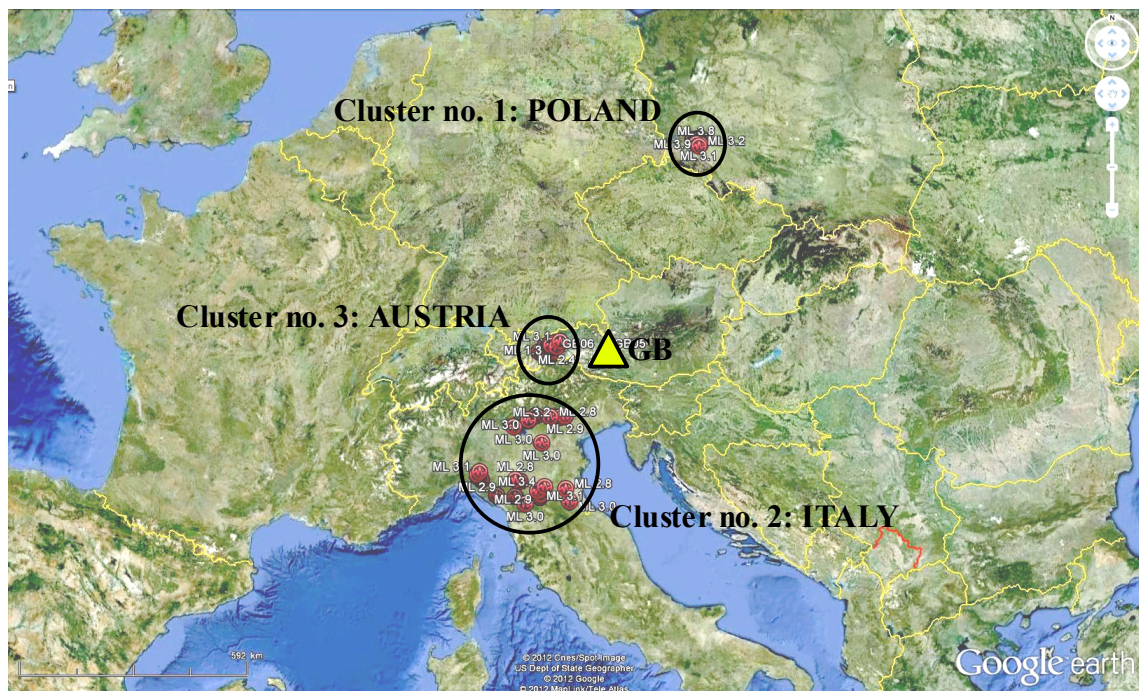


Figure 3.5 spatial distribution of the final dataset

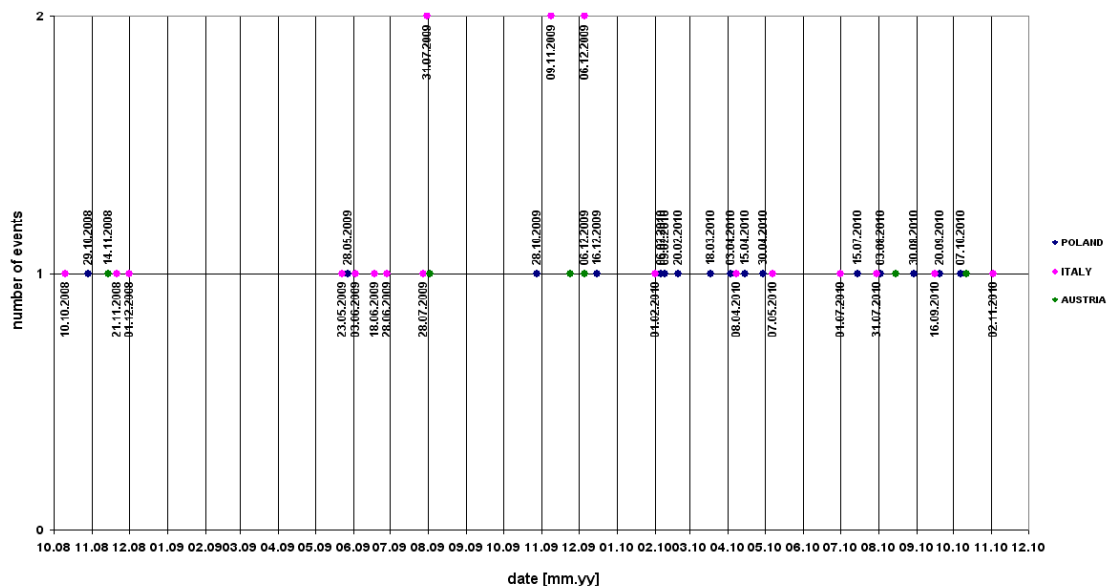


Figure 3.6 temporal distribution of the final dataset

3.2.4. Inverse filtering

The transfer function is an important tool to describe the behaviour of a recording system and to quantify its influence on the output signal obtained. Different seismometers have different transfer functions depending on their damping constants and their corner frequencies and therefore show different filter performances (cf. chapter 6.3).

When wanting to compare signals recorded by different seismometers (e.g. five 4.5 Hz and one 1 Hz seismometer like in this study) it is necessary to reverse the influence of the seismometer on the recorded signal first. Therefore inverse filtering has been applied.

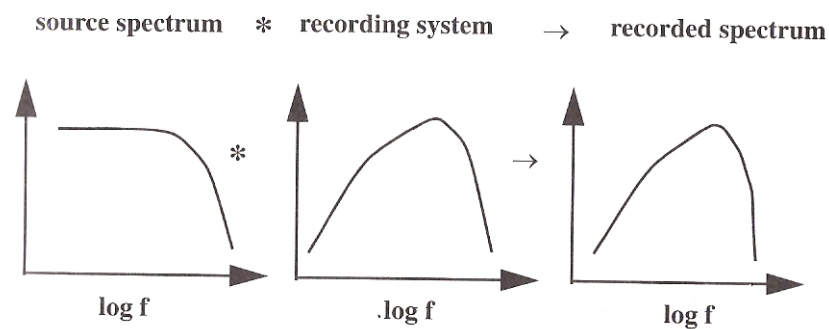


Figure 3.7 Recording the displacement spectrum of an idealized earthquake source

(Source: Scherbaum 2007: 140)

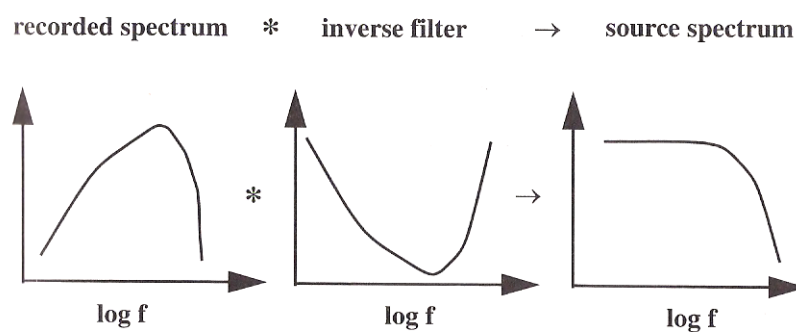


Figure 3.8 Recovering the source spectrum by inverse filtering

(Source: Scherbaum 2007: 141)

The Matlab function $freqs(b,a,w)$ calculates transfer functions of various systems by entering the required filter coefficients. The *filter coefficients* a and b contain information describing the system, such as the *damping* h and the *corner frequency in the undamped case* ω_0 . To translate these parameters into the demanded *filter coefficients* a and b , we will take a look on the transfer function of a seismometer (eq. (6.34)) and the transfer function of a general continuous Nth order LTI system (eq. (6.35)) in the LaPlace domain:

$$T(s) = \frac{-s^2}{s^2 + 2\epsilon s + \omega_0^2}$$

$$T(s) = \frac{\beta_0 + \beta_1 s + \beta_2 s^2 + \dots + \beta_L s^L}{\alpha_0 + \alpha_1 s + \alpha_2 s^2 + \dots + \alpha_N s^N}$$

where $\epsilon = h\omega_0$ is a damping parameter.

Comparing the above equations, introducing a damping of $h = 0.707$ and the corner frequencies $\omega_0 = 1$ Hz and $\omega_0 = 4.5$ Hz respectively will lead to the following expressions for the *filter coefficients* a and b :

$$b = [-1, 0, 0]$$

$$a = [1, 2\epsilon, \omega_0^2]$$

Note: The parameters used for calculation are theoretical values that are not completely the same as the actual damping constants of the seismometers on side but the difference is negligibly small.

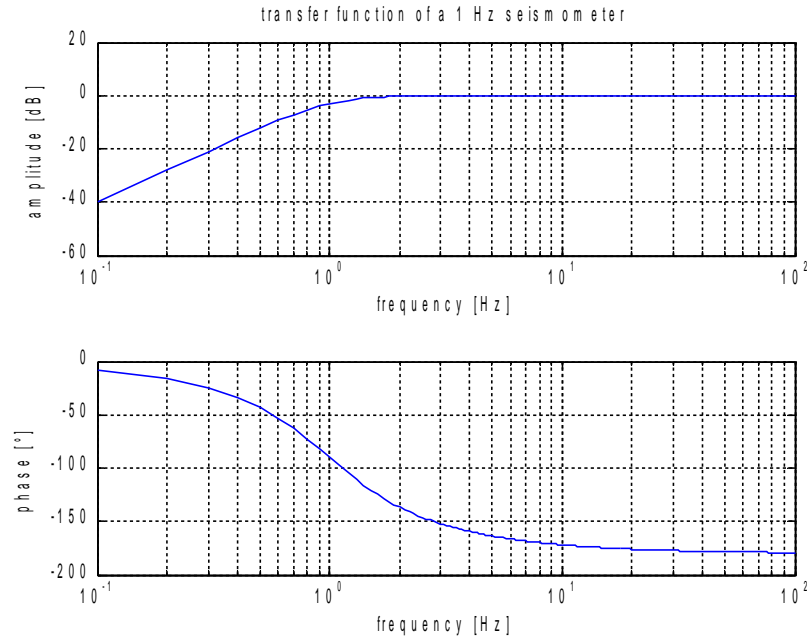


Figure 3.9 transfer function of a 1 Hz seismometer with a damping of 0.707

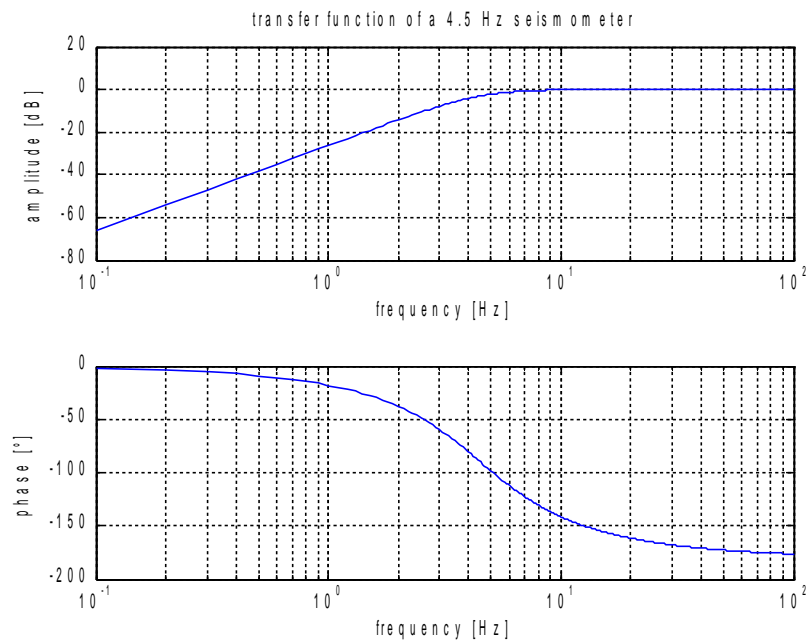


Figure 3.10 transfer function of a 4.5 Hz seismometer with a damping of 0.707

In order to get rid of the instrumental influence it is necessary to reverse what the the transfer function did to the recorded data by creating a new filter that basically consists of the inverse transfer function $H(s) = A(s) / B(s)$.

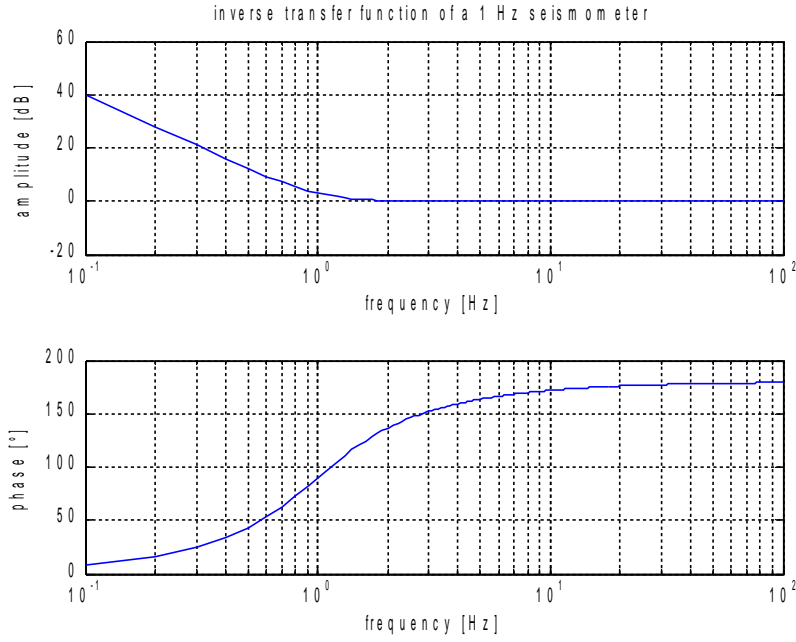


Figure 3.11 inverse transfer function of a 1 Hz seismometer with a damping of 0.707

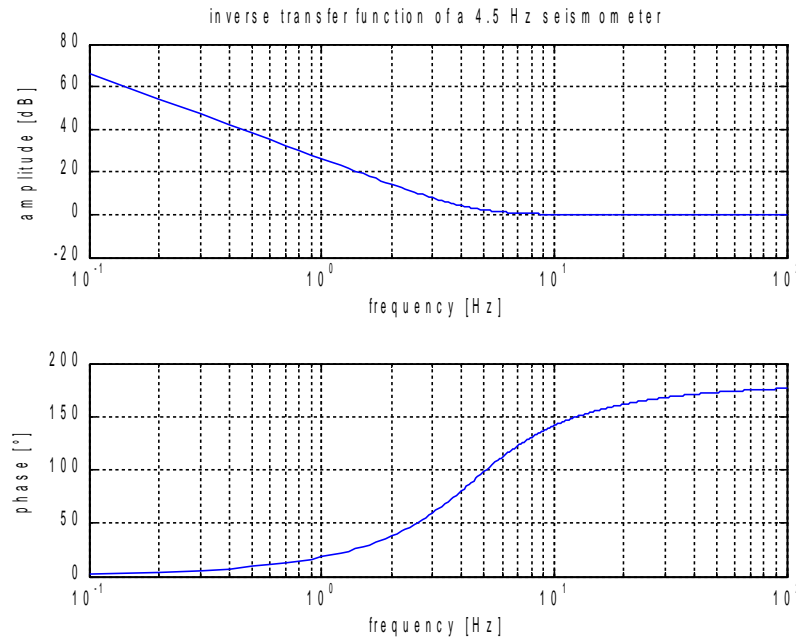


Figure 3.12 inverse transfer function of a 4.5 Hz seismometer with a damping of 0.707

Outside the pass-band of the recording instrument the magnification of the inverse filter is largest which leads to an amplification of noise within that frequency band. Especially the low frequency electronic noise needs to be taken care of. Thus, and to exclude the singularity at $f = 0$ Hz which is part of the denominator as well, a basic 2-pole-butterworth high pass filter with a cutoff frequency $f_c = 0.8$ Hz has been used.

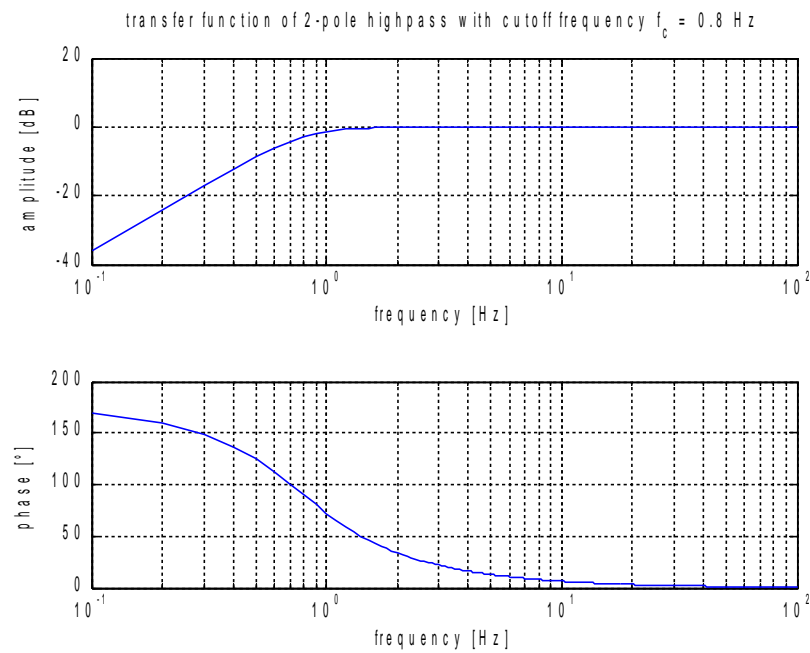


Figure 3.13 transfer function of a 2-pole butterworth highpass with a cutoff frequency of 0.8 Hz

The “analog” filters can be combined either multiplying the transfer functions or convolving the filter coefficients with each other and can then be digitized switching from the s-plane to the z-plane performing a bilinear transform (cf. chapter 6.2.4) using the Matlab function *bilinear(num,den,fs)* and introducing the sampling rate respectively the sampling frequency $fs = 200$ Hz during summer and $fs = 100$ Hz during winter.

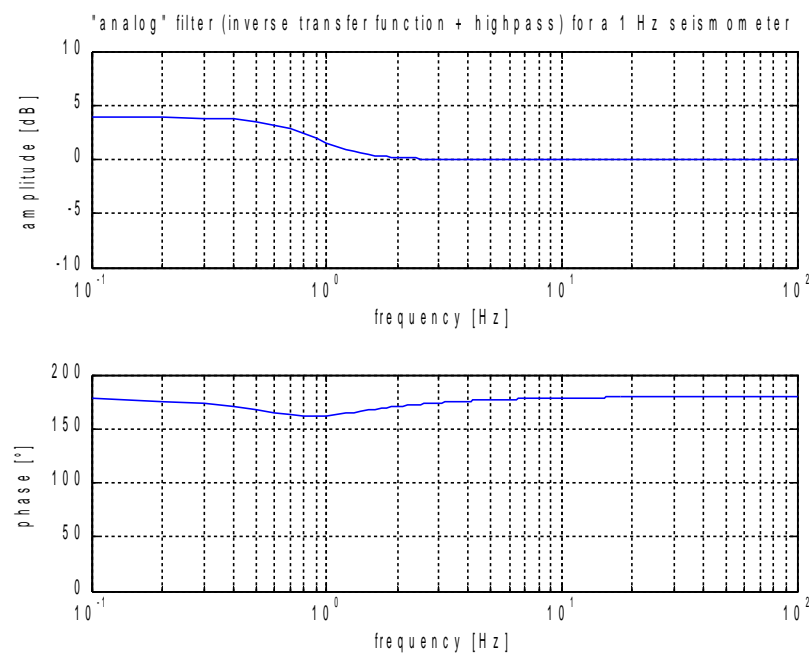


Figure 3.14 "analog" filter consisting of the inverse transfer function of a 1 Hz seismometer and a high-pass with a cut-off frequency of 0.8 Hz.

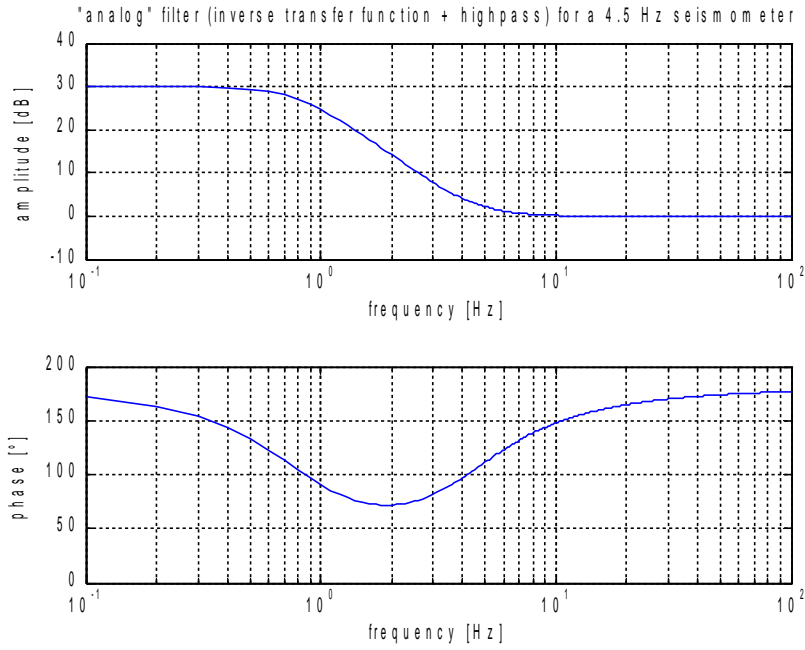


Figure 3.15 "analog" filter consisting of the inverse transfer function of a 4.5 Hz seismometer and a highpass with a cut off frequency of 0.8 Hz

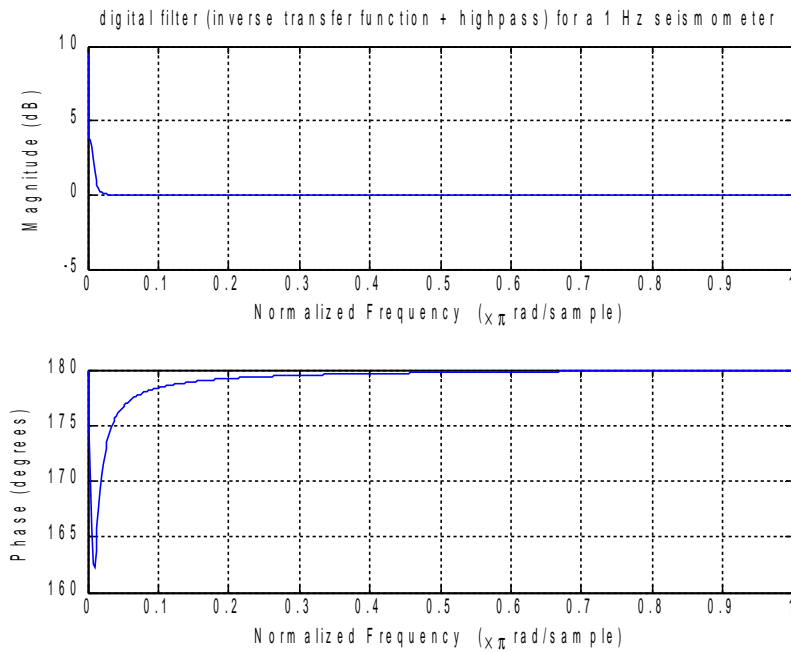


Figure 3.16 bilinear transformed digital filter consisting of the inverse transfer function of a 1 Hz seismometer and a high-pass with a cut-off frequency of 0.8 Hz

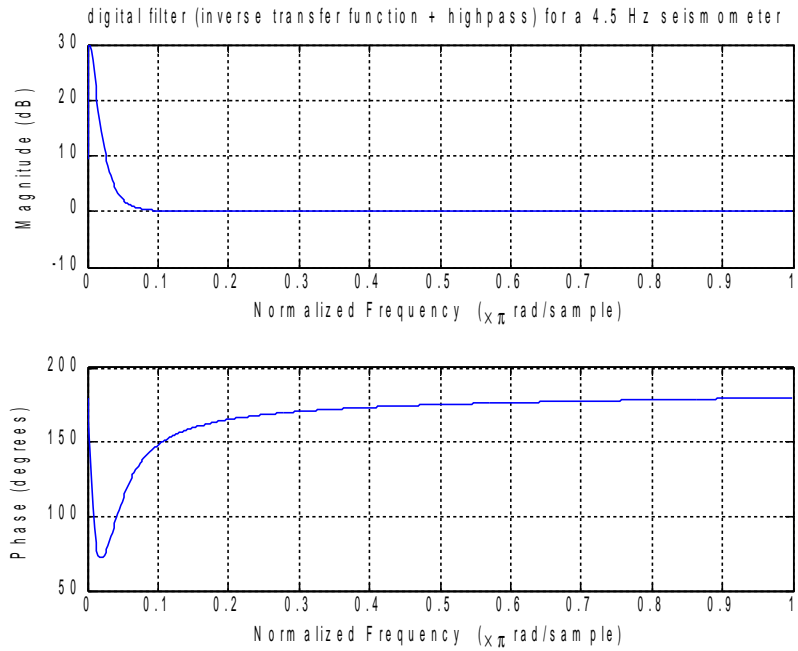


Figure 3.17 bilinear transformed digital filter consisting of the inverse transfer function of a 4.5 Hz seismometer and a high-pass with a cut-off frequency of 0.8 Hz

3.2.5. Data export

After manually sorting out the data that is going to be used for signal correlation, Seismon can export the desired traces to the well known SEG-Y format. The data used for further processing can then be imported again using ProMAX.

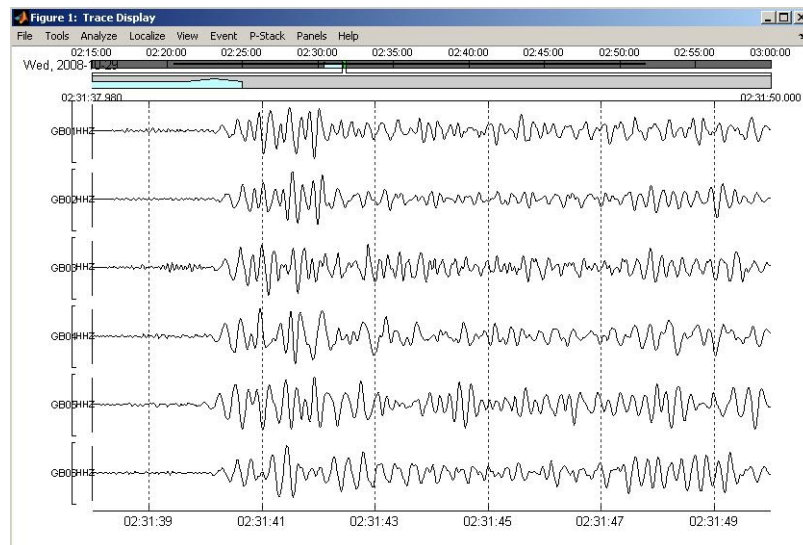


Figure 3.18 exported data (window length: 12 s, start: 2 s before first break)

3.3. Time picking using signal correlations

To carry out signal correlation using one of the stations' signals as reference signal it was decided to export the data and import it again using the well known interactive seismic data processing software, ProMAX. ProMAX offers a comprehensive processing toolkit, including tools such as to cut out parts of different lengths from any trace and to e.g. apply them as a filter later on. Also time picking and exporting the uniquely assigned picks in order to access them with any other software, is easy to handle with ProMAX.⁵

Signal correlation methods could be integrated in Seismon as well, but this was not part of the study.

3.3.1. Data import

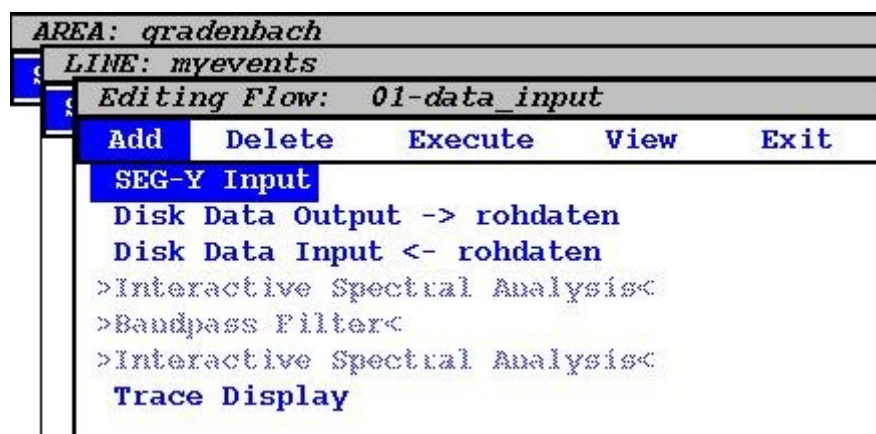


Figure 3.19 ProMax data import

Using the flow shown in figure 3.19, the designated data has been imported again using ProMAX. To determine the travel time differences using signal correlations it is important to limit the frequency content of the signals to a uniform bandwidth. After taking a look on the spectral composition by bringing a tool called *Interactive Spectral Analysis* into action it was decided to apply a bandpass with 20 Hz as upper limit.

⁵ For further information: <http://www.halliburton.com/ps/Default.aspx?navid=221&pageid=862&prodid=MSE%3a%3a1055450737429153> [last downloaded: 2013-02-27]

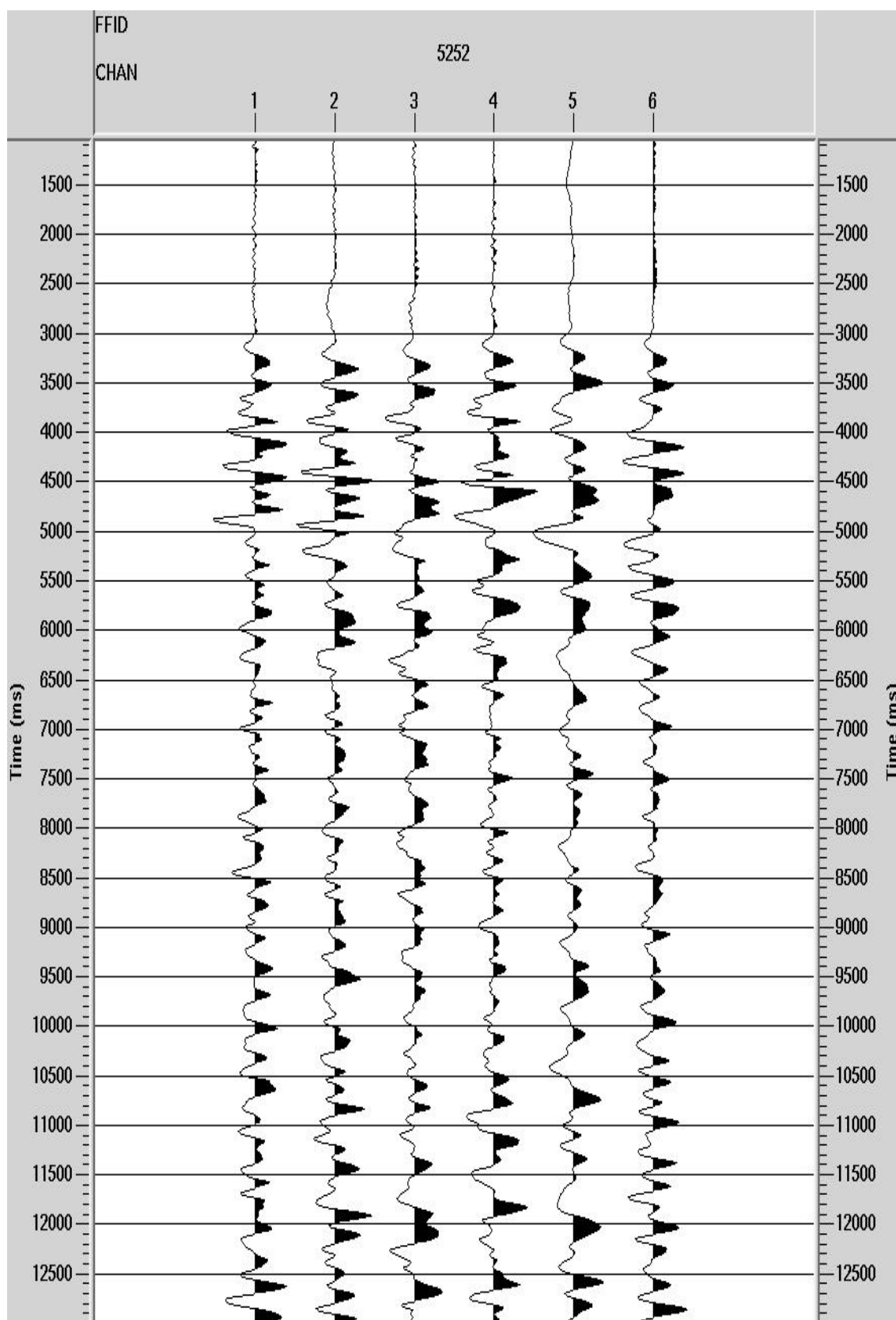


Figure 3.20 "inverse filtered" data with band-pass

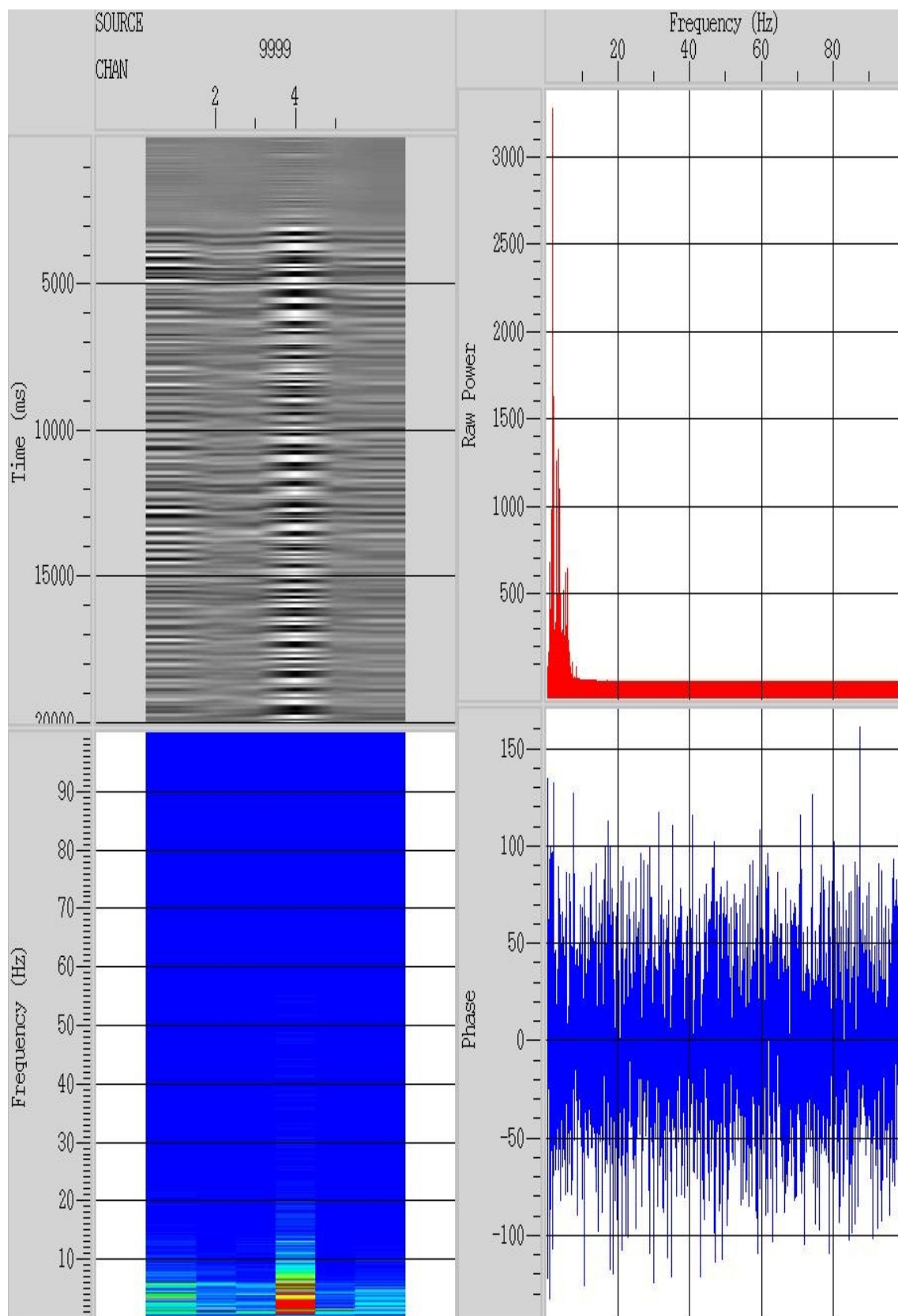


Figure 3.21 spectral analysis of "inverse filtered" data with band-pass

3.3.2. Signal Correlation

As described in chapter 6.4. signal correlation is a powerful tool to reduce noise as well as to find out when and if one signal occurs in another. Since we are interested in travel time differences of waves coming from different events, we will need a reference signal (wavelet) related to the designated event, in order to find out when that signal appears in the individual stations recordings.

The reference signal was chosen to be part of the signal recorded at station GB03, because it was the only station where data was available for all the final events. To get a clearer picture of the first arrival it is adequate to choose correlation windows that include the peak of the first arrival followed by two or three more peaks only. This leads to a variation of window lengths of 400 ms to 800 ms depending on the direction of the incoming waves.

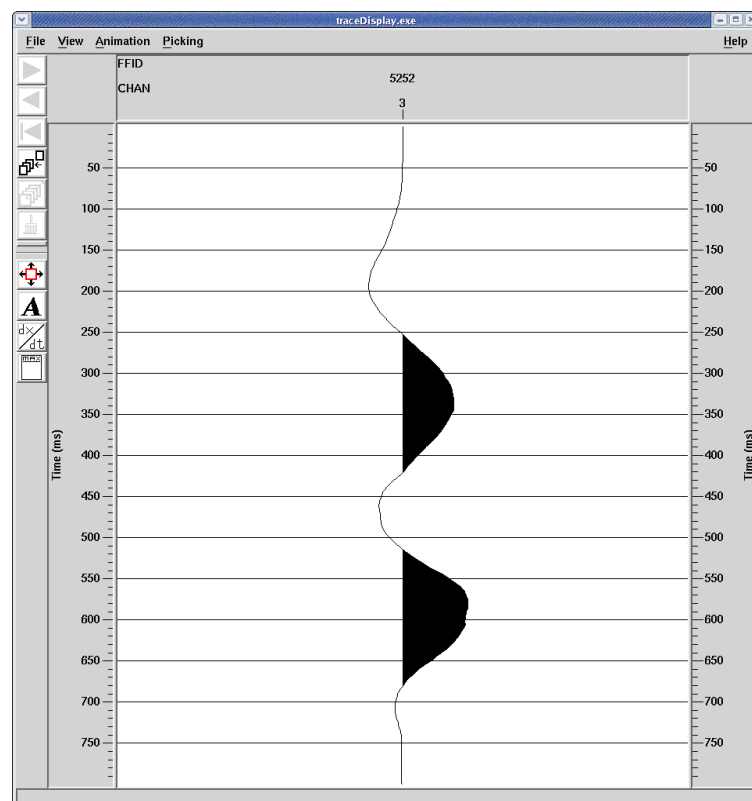


Figure 3.22 an example for a correlation window with 800 ms in length

After conducting the signal correlations the maxima of the auto and cross correlations were manually picked to receive the values of time when maximum correlation of waveforms was attained.

The table containing the field file identifier (FFID), the channels (stations) and the manually picked time values can be exported and later compared to the calculated travel time differences.

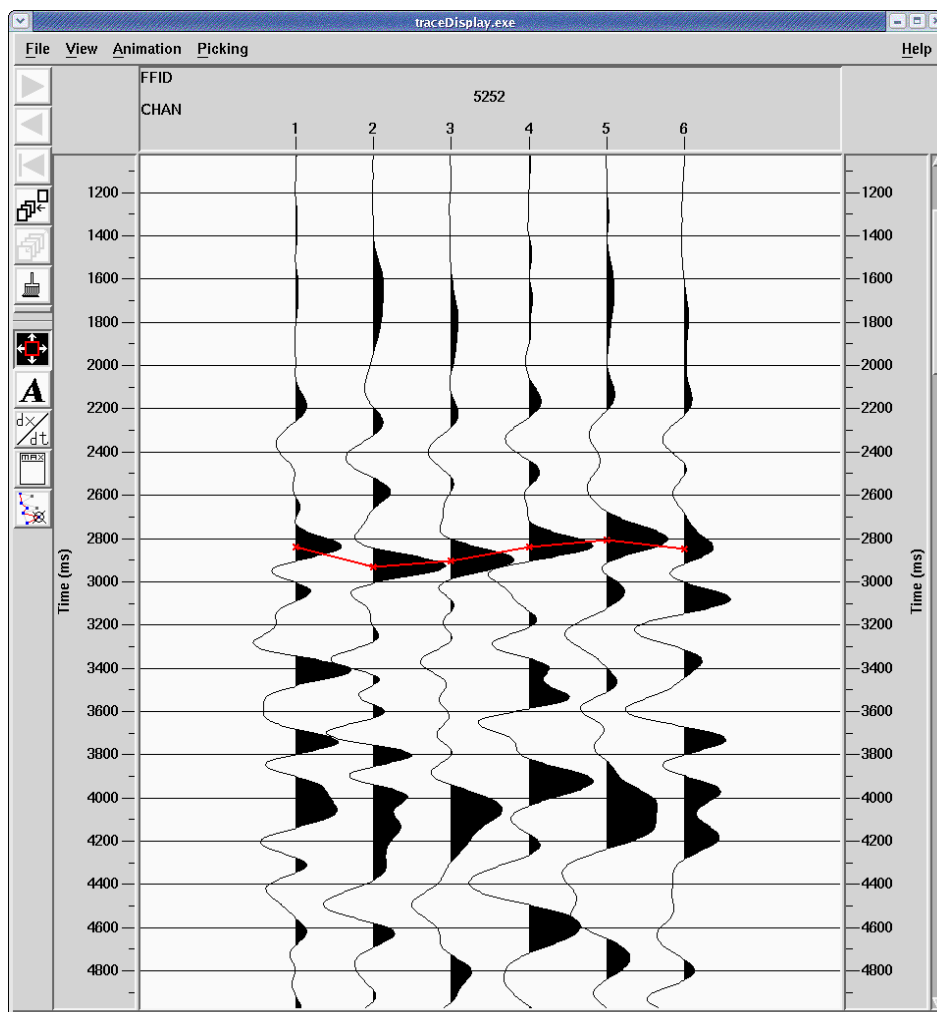


Figure 3.23 picking of maxima of received auto and cross correlations

3.4. Calculating theoretical travel time differences

In order to be able to compare travel times of waves coming from different directions some reductions have to be applied. Thus, theoretical travel time differences have to be calculated. To calculate travel times (or travel time differences) based on the concept of ray theory (cf. chapter 6.5.), we first need to know the so called horizontal slowness or ray parameter p and the "real" distances between the individual stations.

Since dipping layers have an effect on apparent velocities, the dip of the Moho-discontinuity has been taken into account by altering the ray parameter p .

To regard the stations' height differences, vertical travel time differences have to be calculated, using the so called vertical slowness η .

3.4.1. Receiving the ray parameter p using the TauP toolkit

To receive the *ray parameter* p a java based toolbox called "TauP Toolkit" was used. The "TauP Toolkit" is free software, copyrighted by the University of South Carolina and offers a variety of flexible seismic travel time and raypath utilities. Based on a tau-p model of the earth it calculates e.g. arrivals of different phases, returns their names, ray parameters, travel times etc.⁶

In this study the tau-p model was set to be "ak135" and the seismic phase was set to be a first arrival P wave in the crust or mantle. The epi-distances were taken from the calculations using the *distance()* function in chapter 3.2.2.2.. Entries from the earthquake bulletin that included a depth of the source were depth corrected using the *depthCorrect* function of the "TauP Toolkit".

The parameters being returned were the *ray parameter* p (that can also be called horizontal slowness not only after the conversion from [s/rad] in [m/s]) and the *seismic phase*. The corresponding *average apparent velocities* resulted in *8000 m/s* for Pn waves coming from direction Poland and Italy and *5800 m/s* for P waves coming from direction Austria.

The elevation of the stations was not taken into account yet. The stations are at this point all lying in the same plane with $z = 0$.

⁶ For further information: (<http://www.seis.sc.edu/software/TauP/>)

3.4.2. Applied reductions

3.4.2.1. Moho-dip reduction

The Mohorovičić discontinuity, today simply referred to as *Moho*, is the boundary that separates crustal rocks from rocks of the upper mantle. An abrupt increase in velocity is seismically detectable and contributions to the boundary may arise not only from chemical contrasts but also "(...) from transitions in rheological properties, phase transitions in shallow mineral structures, and petrographic fabrics of the rocks." (Lay et al. 1995: 254)

Recognizing the complexity of the crust it is still useful to assess the basic seismological feature of shallow rocks having slower seismic velocities than deeper rocks. Figure 3.24 shows a low-velocity layer over a faster mantle, approximating crustal structure (two subdivisions) in a highly schematic way. (Lay et al. 1995: 252-254)

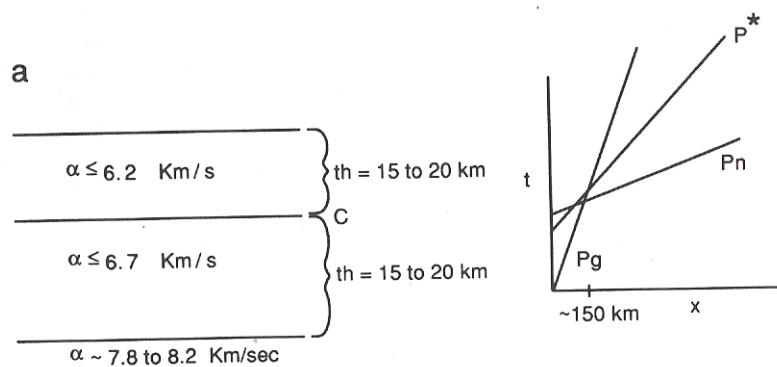


Figure 3.24 generic continental crustal structures and schematic travel time curves where P_g is a wave in the upper crust, P^* is a wave in the lower crust or along the Conrad discontinuity and P_n is a head wave, refracted below the Mohorovičić discontinuity; the 150 km mark the crossover distance

(Source: Lay et al. 1995: 254)

The thickness of continental crust varies from 20 to 70 km. Below the European continent the Moho is quite oblique which has been taken into account as well. To estimate what happens to the *apparent velocity* α and the *ray parameter* p when having a tilted plane instead of a horizontal one, a simple sketch has been drawn that also shows the displacement of the so called *piercing point*. Based on the velocity of 8000 m/s for the Moho and a velocity of 6500 m/s for the crust, one can see that neither

p nor the location of the *piercing point* change significantly with a dip of this order of magnitude. Even when assuming a dip of approximately 10° the piercing point moves "only" 20 km uphill along the slope.

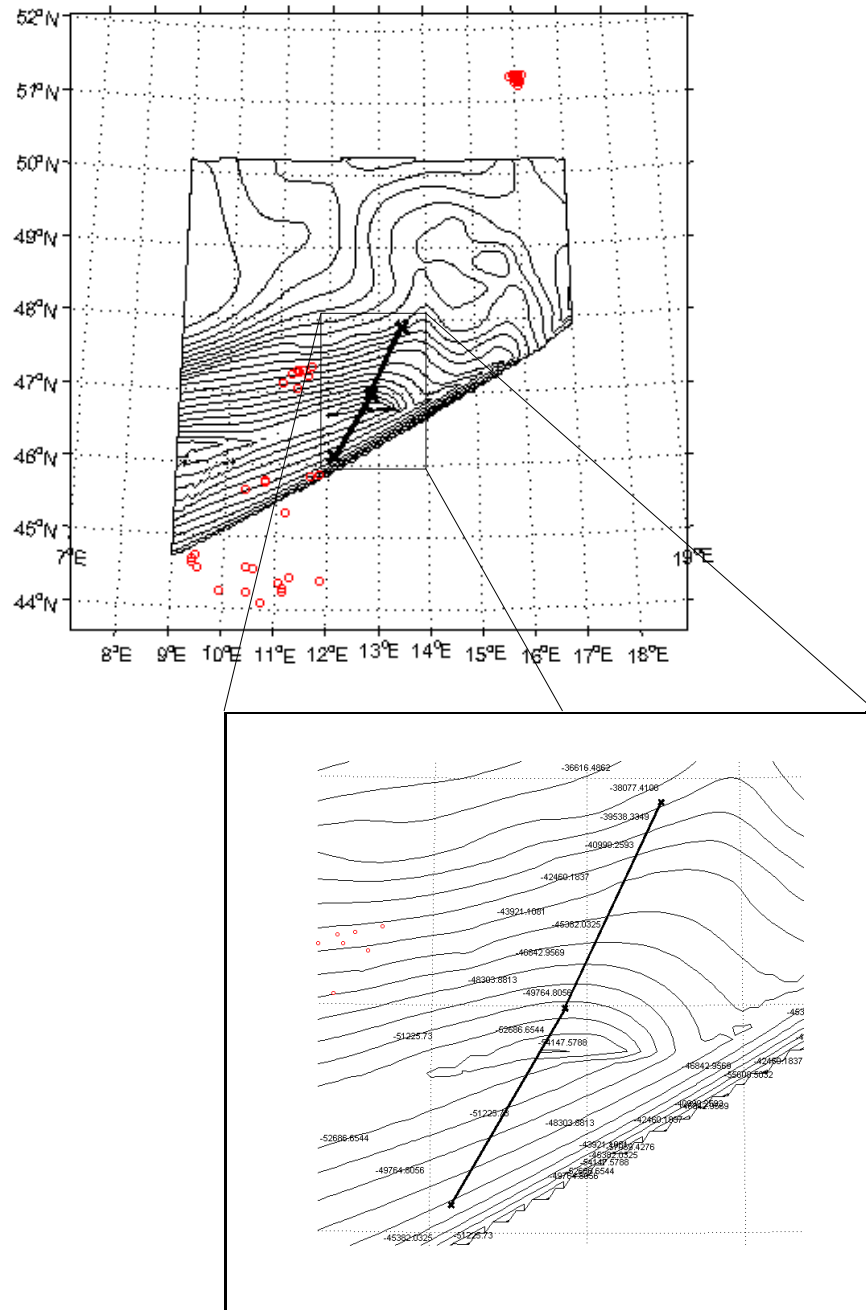


Figure 3.25 central European Moho with lines into direction Poland (25°) and Italy (210°) to estimate the dip of the Moho around the investigation side; the dataset was provided by the Vienna Technical University

Figure 3.25 shows a map of the Mid-European Moho, with lines in the directions of the events having a *Pn wave* (head wave along the Moho) as first arrival. The piercing point is lying within the range of the two lines, therefore the dip can be assumed to be constant. Inserting the values read out off figure 3.25 the dip has been calculated using the simple equation of a line $y = kx + d$ where $k = \Delta y / \Delta x = \Theta$. Δy is the difference in depth of the Moho, Δx is about 110 km.

$$\Theta_{\text{Poland}} \approx 6.5^\circ$$

$$\Theta_{\text{Italy}} \approx 2.7^\circ$$

In presence of dipping layers, head waves have different apparent velocities depending on whether the rays are travelling *updip* or *downdip* (cf. chapter 6.5.2.4.). In this case, the rays are travelling downdip coming from both directions Poland and Italy. Using equation (6.57) for waves travelling downdip, leads to a *new apparent velocity* α .

$$\alpha_{\text{Poland}} \approx 7400 \text{ m/s}$$

$$\alpha_{\text{Italy}} \approx 7700 \text{ m/s}$$

3.4.2.2. Directivity reduction

Since we are interested in calculating travel time differences we need to know the distances between the individual monitoring stations. Based on the assumption that waves reach the stations as wave fronts of a plane wave, the actual distances between the individual stations depend on the incident angle of the wave front at reference station GB03 respectively on the backazimuth being returned when calculating the distance between GB03 and the appropriate event and can therefore not be taken into account directly. The base for a calculation that regards the direction of the propagating wave front is an orthogonal projection where the calculated distances between the stations and station GB03 are being projected onto the direction of propagation (fig. 3.26).

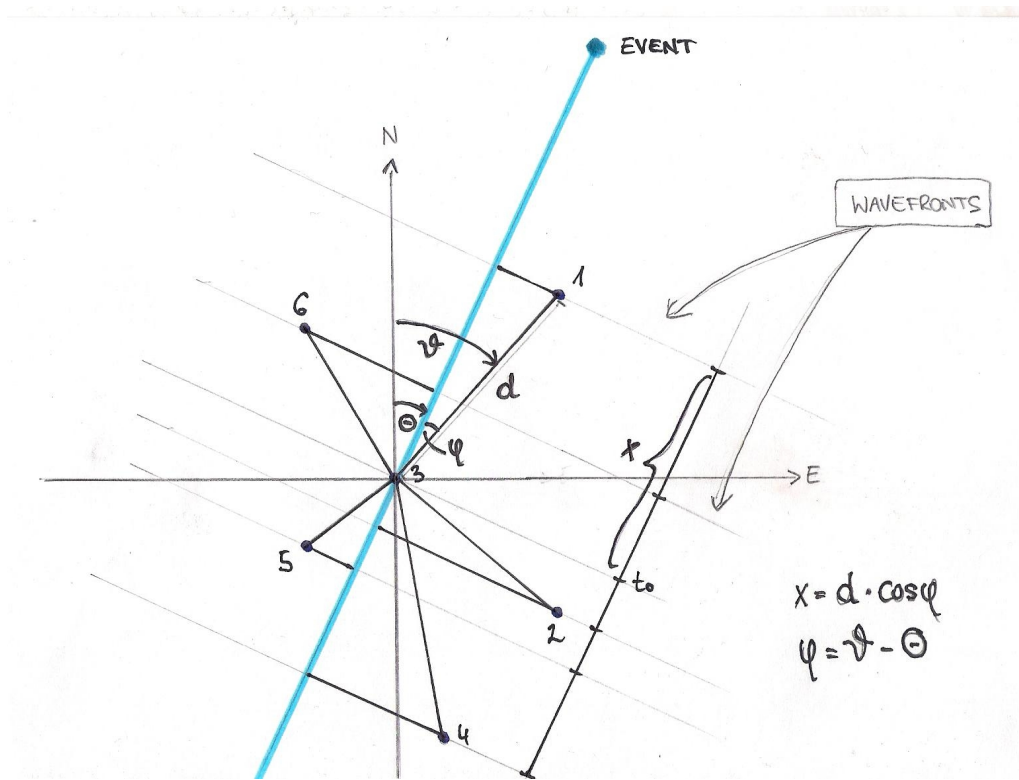


Figure 3.26 sketchy geometrical considerations for a correction of the epicentral distances regarding the direction of propagation of the incident wave front

The horizontal travel time differences can be calculated using the first term of equation (6.52):

$$tt_{Hor} = pX$$

where $p = 1 / \alpha$ (reciprocal of the new apparent velocity α from above) and X is the *new reduced distance* between the corresponding station and the reference station GB03.

Subtracting the calculated values for the horizontal travel times from the picked ones will lead to the following results, where *tdiff obs* (tt_{Obs}) are the *picked values*, and *tdiff calc* (tt_{Hor}) are the *calculated horizontal travel time differences* between the corresponding station and station GB03:

Poland

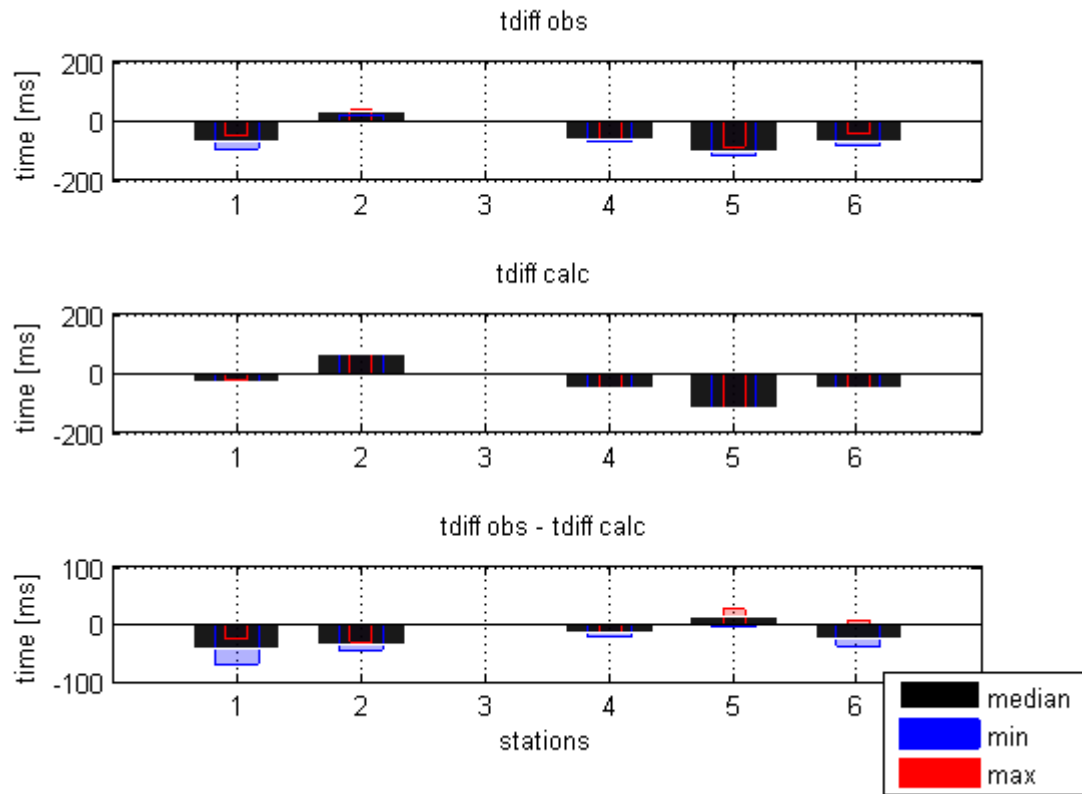


Figure 3.27 horizontal travel time differences (Poland)

	tdiff obs - tdiff calc [ms]		
	Median	Min	Max
GB01	-40	-66	-24
GB02	-35	-43	-30
GB03	0	0	0
GB04	-15	-20	-13
GB05	14	-3	27
GB06	-23	-37	8

Table 3.2 horizontal travel time differences (Poland)

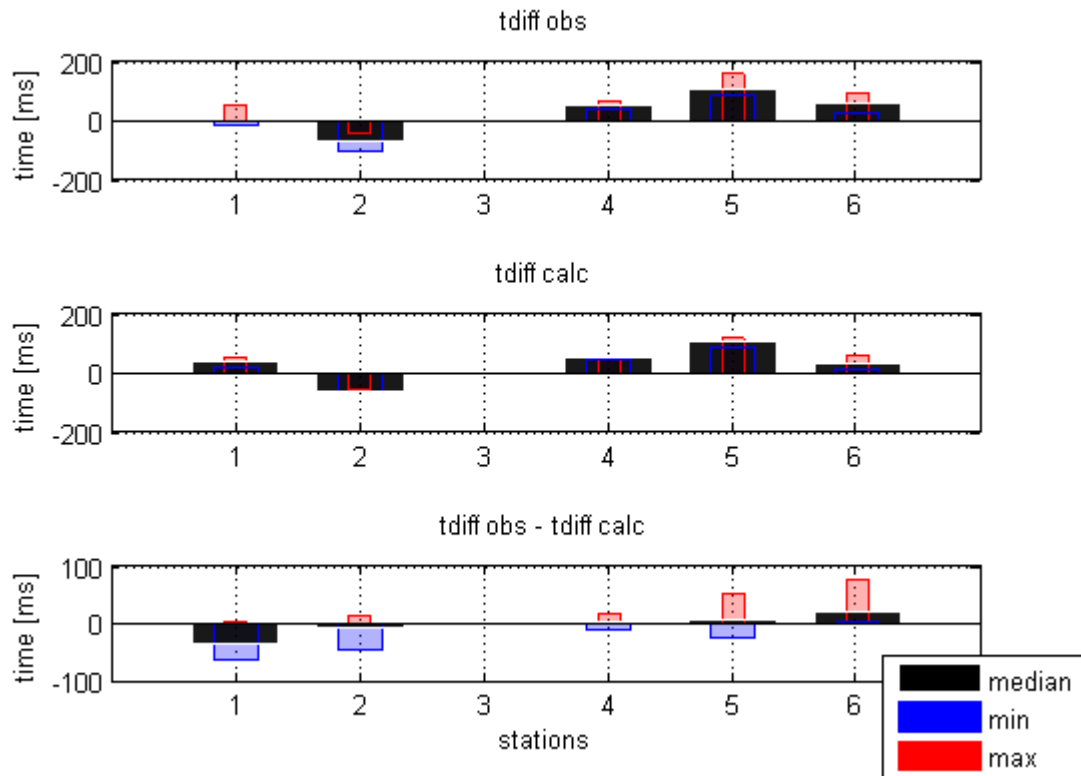


Figure 3.28 horizontal travel time differences (Italy)

	tdiff obs - tdiff calc [ms]		
	Median	Min	Max
GB01	-34	-61	2
GB02	-8	-46	15
GB03	0	0	0
GB04	3	-10	19
GB05	10	-23	51
GB06	19	1	75

Table 3.3 horizontal travel time differences (Italy)

Austria

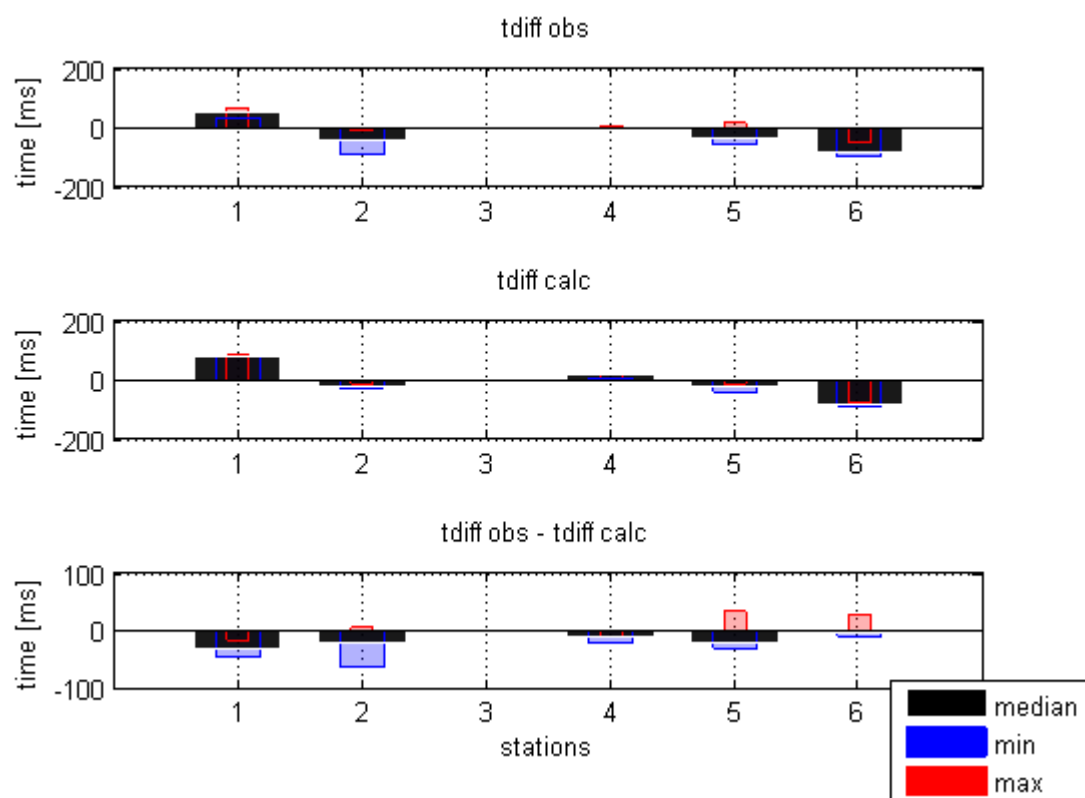


Figure 3.29 horizontal travel time differences (Austria)

	tdiff obs - tdiff calc [ms]		
	Median	Min	Max
GB01	-31	-44	-16
GB02	-23	-62	6
GB03	0	0	0
GB04	-14	-21	-9
GB05	-20	-30	33
GB06	3	-9	26

Table 3.4 horizontal travel time differences (Austria)

3.4.2.3. Height reduction

As described in chapter 6.5.1.1., the vertical travel time depends on the vertical slowness $\eta = (\gamma^2 - p^2)^{1/2}$ only, where $\gamma = 1/\alpha$. To regard the station's heights, an *average velocity* of $\alpha = 4500 \text{ m/s}$ for the solid rock has been assumed (see fig. 2.7). The *ray parameter* p is taken from the calculations above. Using the second term of equation (6.52) and dropping the factor 2 (one-way vertical travel) will return values for the vertical travel time differences:

$$tt_{\text{ver}} = \eta h$$

where due to simplicity reasons h is the *height of the corresponding station above sea level*. To get the travel time differences relatively to reference station GB03, the value at station GB03 has to be subtracted from the others.

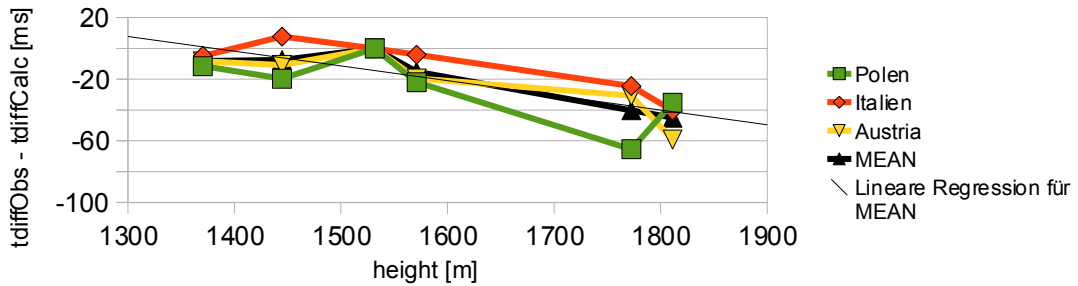


Figure 3.30 plot of travel time residuals over the stations' heights using an average velocity for the solid rock of 4500 m/s

Adding up the travel time residuals for both, the horizontal and the vertical travel path, returns the preliminary results (fig. 3.30). When plotting the results over the stations' heights, one can immediately see that there still is a dependence on height. Therefore the estimated average velocity α has been increased, until the regression line for the mean results turned about horizontal. Inserting an average velocity of $\alpha = 5500 \text{ m/s}$ returned usable results (fig. 3.31).

Since the velocity increases with depth and the ray starts its vertical travel at height $z = 0$, a velocity of 5500 m/s is quite feasible.

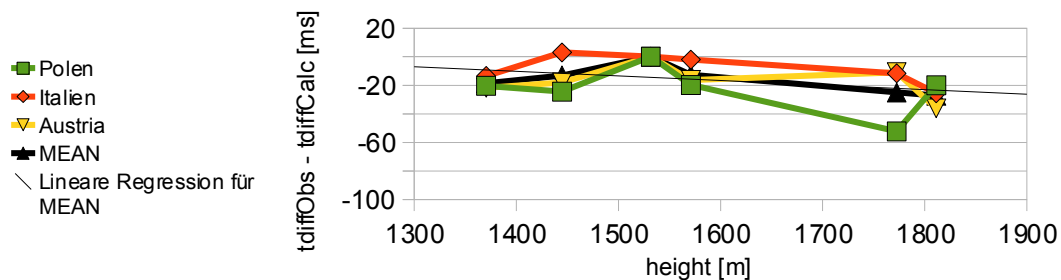


Figure 3.31 plot of travel time residues over the stations' heights using an average velocity for the solid rock of 5500 m/s

		Poland	
	height [m]	$tt_{Obs} - tt_{Hor}$ [ms]	tt_{Ver} [ms]
GB01	1370	-40	-20
GB02	1445	-35	-11
GB03	1532	0	0
GB04	1571	-15	5
GB06	1773	-23	29
GB05	1811	14	34

Table 3.5 vertical travel time differences (POLAND)

		Italy	
	height [m]	$tt_{Obs} - tt_{Hor}$ [ms]	tt_{Ver} [ms]
GB01	1370	-34	-21
GB02	1445	-8	-11
GB03	1532	0	0
GB04	1571	3	5
GB06	1773	19	31
GB05	1811	10	36

Table 3.6 vertical travel time differences (ITALY)

		Austria	
	height [m]	$tt_{Obs} - tt_{Hor}$ [ms]	tt_{Ver} [ms]
GB01	1370	-31	-9
GB02	1445	-23	-5
GB03	1532	0	0
GB04	1571	-14	2
GB06	1773	3	14
GB05	1811	-20	16

Table 3.7 vertical travel time differences (AUSTRIA)

4. Results

Poland

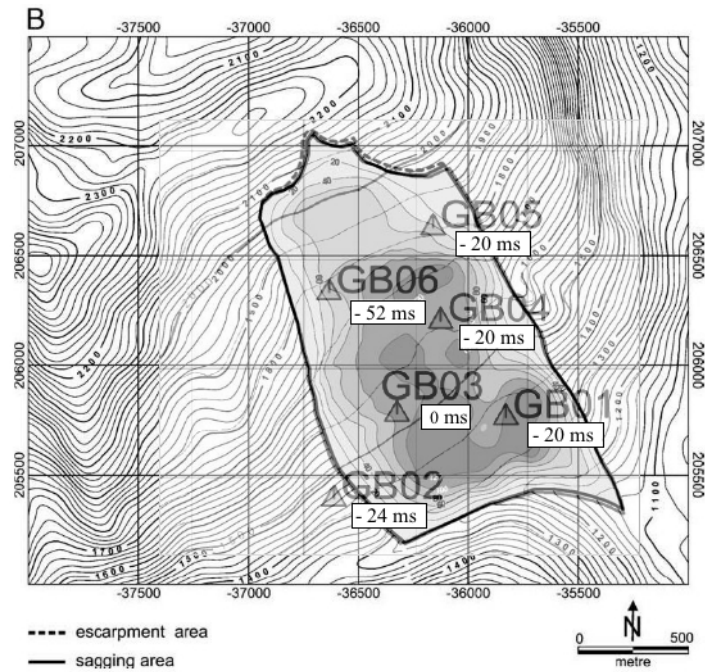


Figure 4.1 final results for "Poland" showing reduced mean travel time differences; the shaded contour plot in the background indicates the thickness of the moving mass

Italy

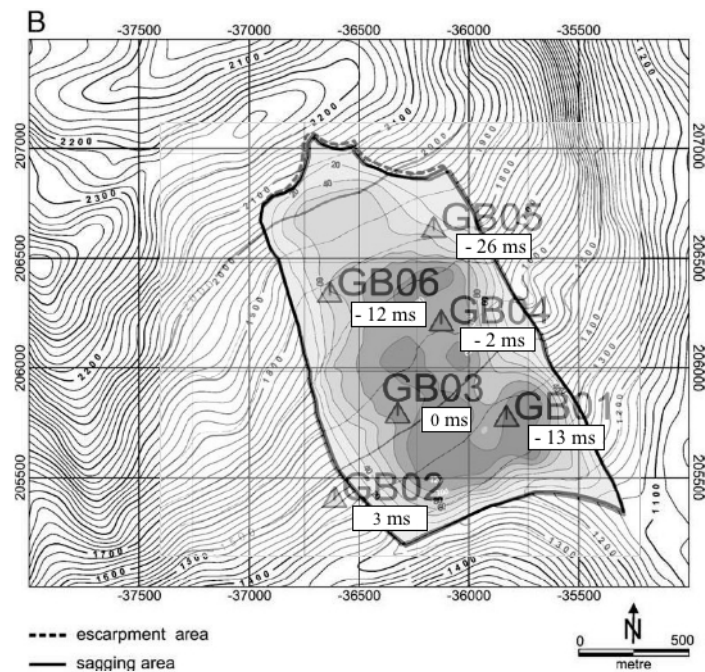


Figure 4.2 final results for "Italy" showing reduced mean travel time differences; the shaded contour plot in the background indicates the thickness of the moving mass

Austria

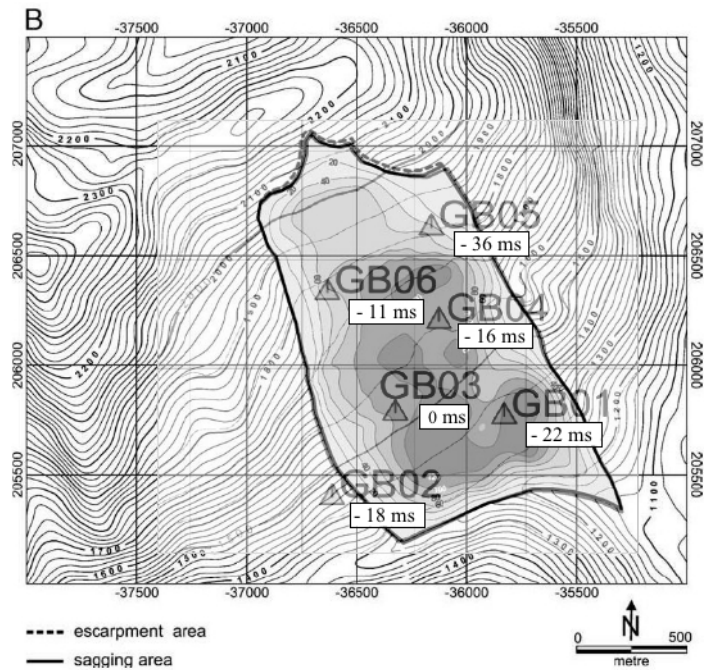


Figure 4.3 final results for "Austria" showing reduced mean travel time differences; the shaded contour plot in the background indicates the thickness of the moving mass

Mean

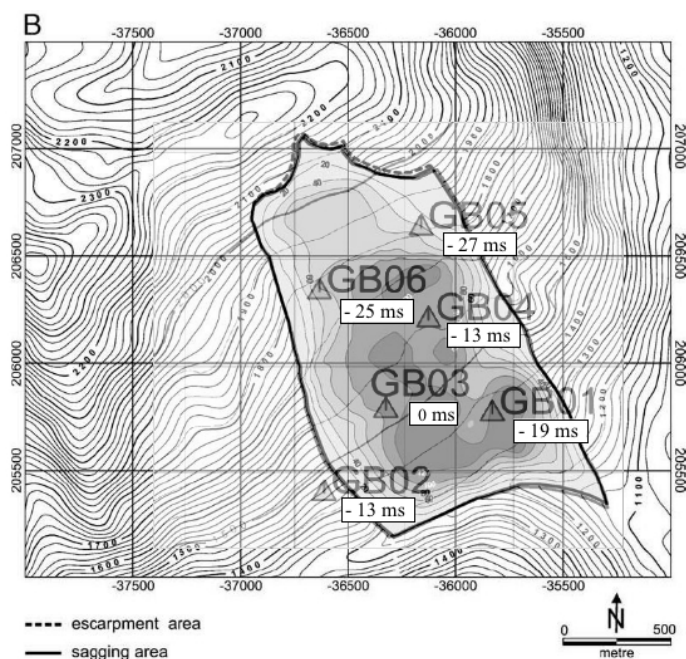


Figure 4.4 final results showing reduced mean travel time differences; the shaded contour plot in the background indicates the thickness of the moving mass

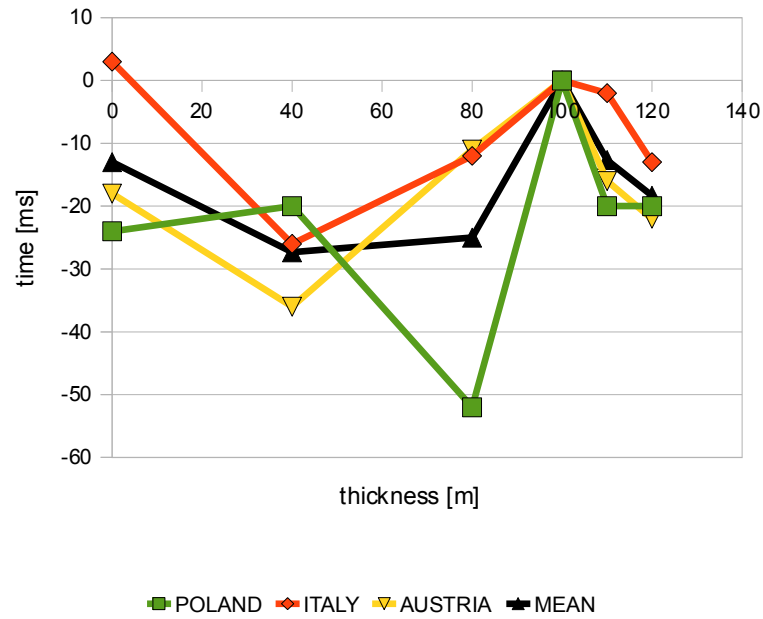


Figure 4.5 final results plotted over the thickness of the moving rock mass

After applying the reductions above to the data observed, almost only negative values remain which means that the travel time differences calculated are bigger than those observed. Obviously the "real" waves spend less time to cover the distances between the individual monitoring stations than the calculated ones which again means that they are travelling at a higher speed than primarily assumed. The waves arrive last at station GB03 in the middle of the landslide where the loosening of the rock mass is large, but unfortunately the accuracy of the results does not satisfy the requirements necessary to draw conclusions on structural changes of the landslide with time.

5. Conclusion

The main aim of this study was to explore if and what kind of information about the Gradenbach landslide can be dragged out by applying the appropriate processing to earthquake data that can be found within the recordings of the put up seismic monitoring network. Thus, signal correlations using near earthquake data, have been carried out and in order to compare travel time differences of waves coming from different directions some reductions have been applied.

5.1. Errors

5.1.1. Time picking

The largest error derives from the signal correlations and the time picking of the correlation maxima afterwards. The correlations have been executed with a reference signal recorded on station GB03. This is quite inconvenient, since GB03 is located in the middle of the landslide and therefore the signals are itself influenced by the loosening of the moving rock mass. However, it was the only recording permanently available and therefore GB03 was chosen to function as reference station.

When excluding errors emerging from common problems in routine hand picking, such as picking the wrong phase etc., the accuracy of the results mainly depends on the similarity of waveforms. The shape of a seismic wavelet is generally affected by multiple components leading to highly complex waveforms. Thus, it is not surprising that waveforms of some of the events appear to be more similar at some stations than others. As a consequence maxima of the cross correlations might not be that definite and therefore not that easy to pick. A change of the correlation window length mainly resulted in a shift of the error which means that e.g. a clear maximum at one station became broad at another while a broad maximum became more distinct. This indicates that it would not be expedient to specify a constant picking error for all the stations and all the events investigated. Nevertheless, an average picking error of about ± 10 ms is regarded as a quite reliable estimate.

5.1.2. Applied reductions

The applied reductions are simple, thus they are a source for further errors as well. It has been assumed that the wave fronts reach the stations as wave fronts of a plane wave. The ray parameter p represents an average value such as the dip of the Moho is an average dip assumed to be constant within the region around the piercing point. The height correction includes an assumed average velocity for the solid rock of 5500 m/s which can be compared to a mass-correction in gravimetry where the density is assumed to be constant and the calculated values are being subtracted from the observed ones.

5.1.3. Statistics

Furthermore it has to be mentioned, that the final results for the three different directions represent mean values of the events investigated (fig. 4.1 - fig. 4.3) while fig. 4.4 represents the mean value of all of the results put together. Sometimes the variation of travel time differences along the horizontal travel path was bigger, sometimes smaller, but all in all showing no trend except the basic trend that the signals arrive earlier at some stations and later at others.

It is important to keep in mind that the final results are an average of all the events investigated, containing all sorts of time differences, so improving the statistical methods or classifying the different events in any way might be a first step towards results of bigger accuracy.

All in all, an average error of about ± 15 ms is regarded as a quite reliable estimate for the final results.

5.2. Outlook

Since the selection of the final events used for signal correlation was made by hand, which might be inconvenient when dealing with an even bigger dataset, it would be necessary to introduce methods, parameters to automatise the data selection and to automatically classify the events.

Due to the large picking-error, first arrival time picking would have to be improved by all means in order to make a clear statement about the structural changes of the landslide with time. To make a clear point using signal correlations, it would be indispensable to establish another reference station, preferably at the foot of the mountain range but outside the area of movement.

Improving the applied corrections by modelling the subsurface in greater detail (e.g. ray tracing), could definitely contribute towards results of bigger accuracy as well.

Replacing the passive sources by active ones and shooting at regular time intervals from a known position, could be another possibility to improve this approach.

6. Theoretical and mathematical background

The mathematical background is mainly taken from Arens et al. 2008 and Lang et al. 2005.

6.1. Transformation of functions - integral transformations

Integral transforms frequently offer a smart way to solve complicated differential- or integral- equations. When carrying out an integral transform, one function is mapped onto another. In general an integral transform can be described by a linear integral operator \mathcal{A} . Looking at a given function $f: D \rightarrow \mathbb{C}$, one will receive the transformed function $\mathcal{A}f$ through a differentiation under the integral sign (Parameterintegral).

$$\mathcal{A}f(s) = \int_D k(t, s) f(t) dt \quad \text{where } s \in G \quad (6.1)$$

By means of f and the term $k: G \times D \rightarrow \mathbb{C}$, the new function $\mathcal{A}f$ is set. The function k is often referred to as the kernel of the integral operator and D is the domain.

If the kernel k and the domain D are given, the integral describes a mapping $\mathcal{A}: V \rightarrow W$ that assigns each function $f \in V$ to a function $\mathcal{A}f$, but only if it is guaranteed that the integrals of functions of the set V do exist. Hence the integral transform is defined by its kernel k and the domain D .

Furthermore to be able to talk about a transform it must be guaranteed that the transform can actually be reversed. That means, that for the operator $\mathcal{A}: V \rightarrow W$ a reverse-mapping $\mathcal{A}^{-1}: W \rightarrow V$ with the properties $\mathcal{A}^{-1} \mathcal{A} = I = \mathcal{A} \mathcal{A}^{-1}$ does exist, where I is the identity, i.e. the mapping, that assigns one function f to the same function f again. (Arens et al. 2008: 1130-1131)

6.1.1. Fourier transform

The Fourier transform is defined by the following equation

$$X(f) = \int_{-\infty}^{\infty} x(t) e^{-j2\pi f t} dt \quad , \quad (6.2)$$

writing the frequency in terms of angular frequency $\omega = 2\pi f$:

$$X(j\omega) = \int_{-\infty}^{\infty} x(t) e^{-j\omega t} dt \quad (6.3)$$

The inverse transform is:

$$x(t) = \frac{1}{2\pi} \int_{-\infty}^{\infty} X(j\omega) e^{j\omega t} d\omega \quad (6.4)$$

(Scherbaum 2007: 97)

6.1.2. LaPlace transform

To a function $f: [0, \infty) \rightarrow \mathbb{C}$, on an interval $J \subseteq \mathbb{R}_{\geq 0}$ the LaPlace transform is defined as the function $\mathcal{L}f: J \rightarrow \mathbb{C}$, that is given through the Parameterintegral

$$\mathcal{L}f(s) = \mathcal{L}(f(t)) = \int_0^{\infty} f(t) e^{-st} dt \quad (6.5)$$

if the integral exists for $s \in J$. (Arens et al. 2008: 1133)

For application the most important property of the LaPlace transform arises from looking at the LaPlace transform of a derivative of a function.

$$\begin{aligned} \mathcal{L}\left(\frac{d}{dt}f(t)\right) &= \int_0^{\infty} e^{-st} \frac{d}{dt}f(t) dt = e^{-st}f(t) \Big|_0^{\infty} - \int_0^{\infty} \left(\frac{d}{dt}e^{-st}\right)f(t) dt = \\ &= -f(0) + s \int_0^{\infty} e^{-st}f(t) dt = -f(0) + s \mathcal{L}(f(t)) \end{aligned} \quad (6.6)$$

with the assumption $\lim_{t \rightarrow \infty} e^{-st}f(t) = 0$ which means that $f(t)$ for $t \rightarrow \infty$ is not growing too strongly. Anyway, if $f(t)$ is LaPlace transformable this has to apply, otherwise the LaPlace transform would be unlimited. (Lang et al. 2005: 423)

6.1.3. z transform

The z transform is the discrete counterpart to the LaPlace transform. While the LaPlace transform can be used to analyse continuous differential equations the z transform can be used to analyse discrete difference equations.

The z transform of a discrete sequence $x[n]$ is defined as:

$$Z(x[n]) = \sum_{n=-\infty}^{\infty} x[n]z^{-n} = X(z) \quad (6.7)$$

where z is a continuous complex variable. (Scherbaum 2007: 107)

6.2. Linear time invariant systems (LTI systems)

In order to understand how filters and LTI-systems etc. work and also why it is of importance to apply inverse and simulation filtering we will start by looking at the behaviour of a very simple filter (electric circuit) consisting of a resistor R and a capacitor C in series.

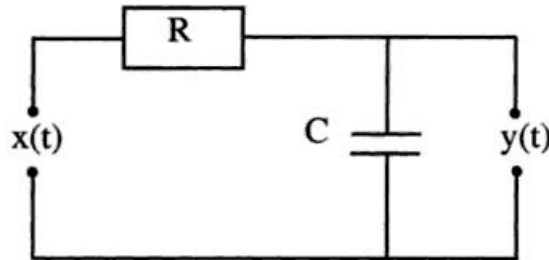


Figure 6.1 RC circuit

(Source: Scherbaum 2007: 12)

It is possible to obtain a differential equation describing the voltage in the circuit by virtually applying a time-dependent input voltage and describing the behaviour of the voltage while the current flows through the resistor R and across the capacitor C :

$$RC \dot{y}(t) + y(t) - x(t) = 0 \quad (6.8)$$

This equation is an example of a first order linear differential equation. It describes the physical properties of the circuit (the corresponding system) and therefore we call it **linear system**.

One important property of linear systems is that if $y_1(t)$ and $y_2(t)$ are the output signals corresponding to the input signals $x_1(t)$ and $x_2(t)$ respectively, the input signal

$$x_3(t) = \alpha_1 x_1(t) + \alpha_2 x_2(t) \quad (6.9)$$

will produce the output signal:

$$y_3(t) = \alpha_1 y_1(t) + \alpha_2 y_2(t) \quad (6.10)$$

Since the properties of the filter (capacitor, resistor) are assumed to be constant in time we call it a **time invariant system** as well.

(Scherbaum 2007: 12-14)

LTI systems can be described by linear differential equations with coefficients constant in time. In the continuous case one could use the LaPlace transform and in the discrete case the z-transform to describe them. (Schurr 2007)

In general one is interested in finding an output that satisfies the temporal differential equation describing the input-output behaviour of a physical system for a given input. A very convenient way to solve differential equations with given initial conditions is the LaPlace transform that converts the differential equations into algebraic equations. One can solve the equation for an output in the LaPlace domain and through inverse LaPlace transform the output function can be transformed back into the time domain. (Schurr 2007)

6.2.1. The frequency response function and the Fourier transform

In signal processing the frequency response function is a very important tool. It allows us to predict a filter's output for any given input signal without further knowledge about the physical processes going on inside the filter. (Scherbaum 2007: 21)

Intuitively one would say that it is easy to find a solution for the above differential equation representing the RC-filter (6.8) when applying an input signal such as a zero input signal $x(t) = 0$. Due to the fact that under very general conditions an arbitrary function can be described as the superposition of harmonics (Fourier!), knowing the output signal of a linear system for a harmonic input signal $x(t) = A_i e^{j\omega t}$ will allow us to obtain the solution for a arbitrary input signal by superimposing the responses for the individual frequencies using the linearity property equations (6.9) and (6.10) and the synthesis equation of the Fourier transform (6.4). (Scherbaum 2007: 14-18)

For a general harmonic signal, equation (6.8) can be solved using the classical trial solution for the output signal:

$$y(t) = A_o e^{j\omega t} \quad (6.11)$$

$$\dot{y}(t) = j\omega A_o e^{j\omega t} \quad (6.12)$$

Inserting this in equation (6.8) we obtain:

$$A_o e^{(j\omega t)} (RCj\omega + 1) = A_i e^{(j\omega t)} \quad (6.13)$$

Relating the amplitude of the output signal to the amplitude of the input signal will lead to a first expression of the frequency response function:

$$\frac{A_o}{A_i} = \frac{1}{RCj\omega + 1} = T(j\omega) \quad (6.14)$$

Altogether when having a harmonic input signal $x(t)$ the corresponding output signal from (6.14) is $y(t) = A_o e^{(j\omega t)}$ with

$$A_o = T(j\omega) \cdot A_i \quad (6.15)$$

where $T(j\omega)$ is the frequency response function. (Scherbaum 2007: 18-19)

When having an harmonic input signal the output of the filter is again an harmonic signal with different amplitude and phase but with the same frequency. This property can also be found in the eigenvector concept of linear algebra, with the values of the frequency response function being the eigenvalues of the system and the harmonic functions being the corresponding eigenvectors. In a linear transformation an eigenvector is transformed onto itself, it does not change direction or compared to the concept of harmonic signals: the frequency content of the signal does not change. (Scherbaum 2007:19–20)

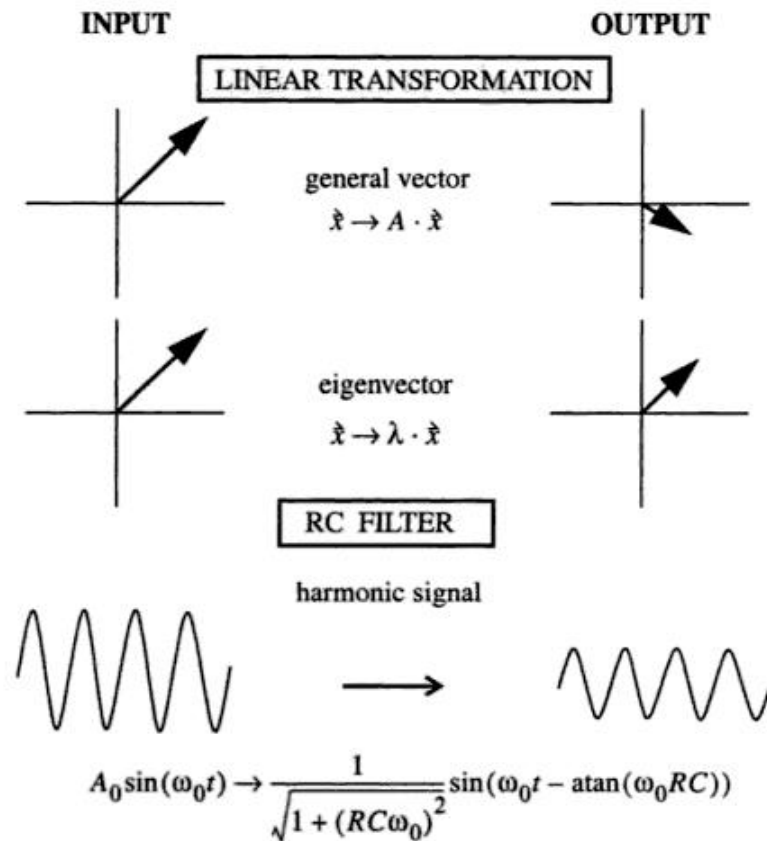


Figure 6.2 Frequency response function and the eigenvector/eigenvalue concept.

(Source: Scherbaum 2007: 20)

Since $A_i(j\omega)$ and $A_o(j\omega)$ can be visualized as the corresponding harmonic components of the input and the output signal's Fourier spectra $X(j\omega)$ and $Y(j\omega)$ respectively, the spectra are related to each other by the frequency response function. (Scherbaum 2007: 20)

$$T(j\omega) = \frac{Y(j\omega)}{X(j\omega)} \quad (6.16)$$

"The properties of an arbitrary linear filter are uniquely described by its frequency response function. In general, the Fourier spectrum of a signal which has passed through a filter is obtained by multiplying (complex multiplication) the Fourier spectrum of the input signal by the frequency response function of the filter." (Scherbaum 2007: 21)

6.2.2. The transfer function and the LaPlace transform

Sometimes the term frequency response function is also referred to as transfer function. Their concepts are closely related to each other but they are not the same thing. We can solve the differential equation (6.8) using the Laplace transform of a function (6.5). This is very convenient since the derivative in the time domain corresponds to a multiplication with the complex variable $s = \sigma + j\omega$ in the LaPlace domain (6.6). (Scherbaum 2007: 21)

Transforming equation (x.x) and dividing the LaPlace transformed output signal by the LaPlace transformed input signal will lead to the following expression for the transfer function of a linear RC filter:

$$T(s) = \frac{Y(s)}{X(s)} = \frac{1}{1+sRC} = \frac{1}{1+s\tau} \quad (6.17)$$

For $s = -1/\tau$ the transfer function $T(s)$ grows to infinity and therefore $T(s)$ has a so called **pole** at this location. (Scherbaum 2007: 22)

"We will see in the following that the existence and the position of a pole at $s = s_p = -1/\tau$ are sufficient to describe most of the properties of the transfer function." (Scherbaum 2007: 22)

6.2.3. The impulse response function

At this point I only want to summarize some core statements regarding the impulse response function:

The impulse response function $h(t)$ is defined as the response of a filter to an impulsive input signal represented by a Dirac delta function $\delta(t)$. (Scherbaum 2007: 24)

The Dirac delta function

The Dirac delta function is not a function in the usual mathematical sense but a singular distribution since it cannot be defined by means of a local integrable function. It is a synthetic product that only under the integration sign has the following formal significance (Lang et al. 2005: 449-450):

$$\int_a^b dt \delta(t-t_0) \equiv \begin{cases} 1 & a < t_0 < b \\ 0 & \text{sonst} \end{cases} \quad (6.18)$$

$$\int_a^b dt f(t) \delta(t-t_0) \equiv \begin{cases} f(t_0) & a < t_0 < b \\ 0 & \text{sonst} \end{cases}, \quad (6.19)$$

where (6.19) can be regarded as a convolution of the delta function with a function $f(t)$. The delta function somehow reveals the integration and substitutes the integral for the value of the integrand at a certain position but only if lying within the range of integration. (Lang et al. 2005: 450)

Using the important property that both, the LaPlace and the Fourier transform of the delta function equals 1 and using the definitions of the frequency response function (6.16) and the transfer function (6.17) will lead to the following statements:

"The frequency response function $T(j\omega)$ is the Fourier transform of the impulse response function." (Scherbaum 2007: 25)

$$T(j\omega) = \frac{Y(j\omega)}{X(j\omega)} = \frac{Y(j\omega)}{1} = H(j\omega) \quad \text{for } x(t) = \delta(t) \quad (6.20)$$

"The transfer function $T(s)$ is the Laplace transform of the impulse response function." (Scherbaum 2007: 25)

$$T(s) = \frac{Y(s)}{X(s)} = \frac{Y(s)}{1} = H(s) \quad \text{for } x(t) = \delta(t) \quad (6.21)$$

6.2.4. Bilinear transform

If the continuous transfer function of a recording system is known as a rational function, it is convenient to approximate the discrete transfer function $T(z)$ from the continuous one $T(s)$ by carrying out a mapping procedure called bilinear transform.

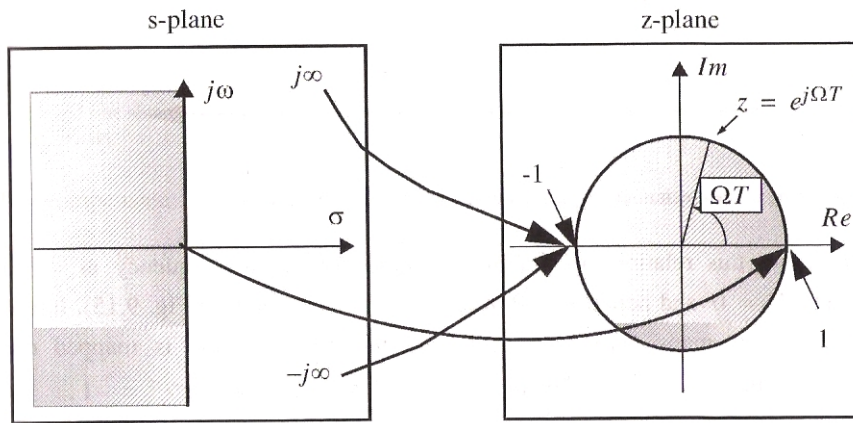


Figure 6.3 mapping of the complex s-plane onto the complex z-plane; the imaginary axis is mapped onto the unit circle, the right half s-plane onto the outside of the unit circle and the left half s-plane onto the interior of the unit circle in the z-plane

(Source: Scherbaum 2007: 157)

The transform is defined as

$$s = \frac{2}{T} \cdot \frac{1 - z^{-1}}{1 + z^{-1}} \quad (6.22)$$

with the sampling interval T and the variables of the complex s- and z-planes, s and z respectively while the inverse transform is given by

$$z = \frac{1 + (T/2)s}{1 - (T/2)s} \quad (6.23)$$

Setting $s = \sigma + j\omega$ in equation 6.23 leads to

$$z = \frac{[2/T + \sigma] + j\omega}{[2/T - \sigma] - j\omega} \quad (6.24)$$

The values of the discrete transfer function $T(z)$ become

$$T(z) = T(s) \Big|_{s=(2/T)[(1-z^{-1})/(1+z^{-1})]} \quad (6.25)$$

(Scherbaum 2007: 156-163)

6.3. The seismometer – an example for a LTI

A simple vertical pendulum seismometer consists of a mass, a spring and a damping mechanism also referred to as dashpot. Through the spring and the dashpot the mass is connected to a frame and the frame itself is fixed relative to the ground. The motion of the mass relatively to the frame can be described by the mass position $x_r(t)$, and the motion of the mass relatively to the ground by $u_m(t)$.

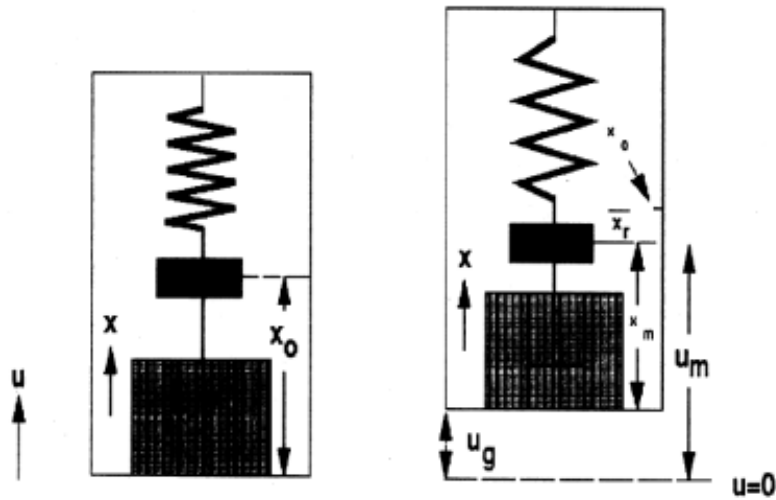


Figure 6.4 vertical pendulum seismometer

(Source: Scherbaum 2007: 49)

The forces acting on the mass and controlling the movements are the following:

- The inertia of the mass:

$$f_i = -m \ddot{u}_g(t) \quad (6.26)$$

where $\ddot{u}_g(t)$ is the acceleration of the ground

- The spring:

$$f_{sp} = -k x_r(t) \quad (6.27)$$

where k is the spring constant

- The dashpot:

$$f_f = -D \dot{x}_m(t) \quad (6.28)$$

where D is the friction coefficient

Using the fact, that in equilibrium these forces add up to zero one can set up the following equation of motion:

$$\ddot{x}_r(t) + \frac{D}{m} \dot{x}_r(t) + \frac{k}{m} x_r(t) = -\ddot{u}_g(t) \quad (6.29)$$

or

$$\ddot{x}_r(t) + 2\epsilon \dot{x}_r(t) + \omega_0^2 x_r(t) = -\ddot{u}_g(t) \quad (6.30)$$

where $\omega_0 = k/m$ is the natural frequency of the undamped system and

$2\epsilon = D/m = 2h\omega_0$ is a damping parameter. (Scherbaum 2007: 48-50)

6.3.1. Frequency response function of a seismometer

To retrieve the frequency response function of the seismometer one can look in more detail at how the system reacts when having an harmonic input signal. This is very revealing since most functions can be described as the superposition of harmonics (Fourier!):

When having a harmonic input signal $u_g(t) = A_i e^{j\omega t}$ with the ground acceleration $\ddot{u}_g(t) = -\omega^2 A_i e^{j\omega t}$ corresponding to it equation (6.30) becomes:

$$\ddot{x}_r(t) + 2\epsilon \dot{x}_r(t) + \omega_0^2 x_r(t) = \omega^2 A_i e^{j\omega t} \quad (6.31)$$

The approach to solving the equation again is a harmonic function:

$$x_r(t) = A_o e^{j\omega t}, \quad \dot{x}_r(t) = j\omega A_o e^{j\omega t}, \quad \ddot{x}_r(t) = -\omega^2 A_o e^{j\omega t}$$

The frequency response function then derives from the ratio between the amplitudes of the input and the output signal:

$$\frac{A_o}{A_i} = \frac{\omega^2}{\omega_0^2 - \omega^2 + j2\epsilon\omega} = T(j\omega) \quad (6.32)$$

(Scherbaum 2007: 60-61)

6.3.2. Transfer function of a seismometer

To obtain an expression for the transfer function of the seismometer the LaPlace transform can be used to solve equation (6.30) based on the following initial conditions:

- starting displacement: $x_r(0) = x_{r0}$
- mass is at rest at time $t = 0$: $\dot{x}_r(0) = 0$
- ground excitation is zero: $\ddot{u}_g(t) = 0$

The LaPlace transform of equation (6.31) is:

$$s^2 X_r(s) + 2\epsilon s X_r(s) + \omega_0^2 X_r(s) = -s^2 U_g(s) \quad (6.33)$$

and therefore the transfer function of the seismometer is:

$$T(s) = \frac{X_r(s)}{U_g(s)} = \frac{-s^2}{s^2 + 2\epsilon s + \omega_0^2} \quad (6.34)$$

When zeroizing σ in $s = \sigma + j\omega$ or replacing s by $j\omega$ in simple terms, the frequency response function can directly be obtained from the transfer function. (Schurr 2007, Scherbaum 2007: 51-63)

The transfer functions of standardized seismometer-galvanometer systems can be effectively approximated by a rational transfer function of the form

$$T(s) = \left(\frac{\beta_L}{\alpha_N} \right) \frac{\prod_{k=1}^L (s - s_{0k})}{\prod_{k=1}^N (s - s_{pk})} = \frac{\beta_0 + \beta_1 s + \beta_2 s^2 + \dots + \beta_L s^L}{\alpha_0 + \alpha_1 s + \alpha_2 s^2 + \dots + \alpha_N s^N} \quad (6.35)$$

representing a general continuous Nth order LTI system with s_{0k} and s_{pk} the k-th zero and pole, respectively. (Scherbaum 2007: 173, 187)

6.4. Correlation

The correlation of two random processes $x(m_1)$, $y(m_2)$ is defined as:

$$\begin{aligned} r_{xy}(m_1, m_2) &= \mathcal{E}[x(m_1)y(m_2)] \\ &= \int_{-\infty}^{\infty} \int_{-\infty}^{\infty} x(m_1)y(m_2)f_{x(m_1)y(m_2)}(x(m_1), y(m_2))dx(m_1)dy(m_2) \end{aligned} \quad (6.36)$$

where $f_{x(m_1)y(m_2)}(x(m_1), y(m_2))$ is the joint probability density function, giving the likelihood of two or more variables assuming certain states or values.

For processes with a time invariant covariance (wide-sense stationary process), the correlation function only depends on the time difference $k = m_1 - m_2$, called cross correlation lag. (Vaseghi 2008: 83)

$$r_{xy}(m_1 + \tau, m_2 + \tau) = r_{xy}(m_1, m_2) = r_{xy}(m_1 - m_2) = r_{xy}(k) \quad (6.37)$$

The correlation method can be used to determine where (or if) a signal occurs in another signal. It uses two different input signals to produce a third one which is then called *cross correlation*. If a signal is correlated with itself it is called *autocorrelation* instead. (Smith 2003: 37)

"The amplitude of each sample in the cross-correlation signal is a measure of how much the received signal resembles the target signal, at that location. This means a peak will occur in the cross-correlation signal for every target signal that is present in the received signal. In other words, the value of the cross-correlation is maximized when the target signal is aligned with the same features in the received signal." (Smith 2003: 138)

6.4.1. Noise reduction

A common problem in signal processing is to extract the signal of interest from the recorded one, which is buried in noise. Compared to the spectrum of white noise (all frequencies) the actual signal spectrum mainly consists of lower frequency components. Since these two spectra overlap, it is necessary to find a way how to separate them.

Since random noise looks a certain amount like any arbitrary target signal it is impossible not to have any noise on the cross correlation signal if there is noise on the

received signal, but except for this noise the peak generated is symmetrical even if the target signal is not. Knowing the shape of the target signal, the correlation method produces an output where the top of the peak is farther above the residue noise than provided by any other linear filter. (Smith 2003: 307-309)

6.4.2. Time delay estimation

The cross correlation of two signals $y_1(m)$ and $y_2(m)$, each composed of an information bearing signal $x(m)$ and an additive noise $n_1(m)$ and $n_2(m)$, given by

$$y_1(m) = x(m) + n_1(m) \quad (6.38)$$

$$y_2(m) = Ax(m - D) + n_2(m) \quad (6.39)$$

looks as follows:

$$\begin{aligned} r_{y_1 y_2}(k) &= \mathcal{F}[y_1(m)y_2(m+k)] \\ &= \mathcal{F}[(x(m) + n_1(m))[Ax(m - D + k) + n_2(m+k)]] \\ &= Ar_{xx}(k - D) + r_{xn_2}(k) + Ar_{xn_1}(k - D) + r_{n_1 n_2}(k) \end{aligned} \quad (6.40)$$

where A is an amplitude factor and D is a time delay variable.

Assuming that signal and noise are uncorrelated (random noise is uncorrelated anyway), all terms besides the first one drop out. (Vaseghi 2008: 84)

$$r_{y_1 y_2} = Ar_{xx}(k - D) \quad (6.41)$$

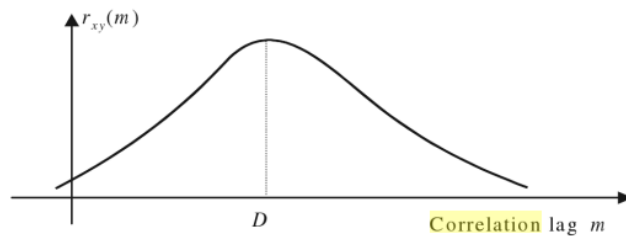


Figure 6.5 The cross correlation function has its maximum at lag D which corresponds to the time delay in demand

(Source: Vaseghi 2008: 84)

6.5. Ray theory

The chapter about ray theory is mainly taken from: Lay et al. 1995.

The basis of almost all body-wave interpretation is the concept of rays. Although this concept is limited to smaller wavelengths (smaller than a few hundred kilometres) and only slowly varying seismic velocities, rays can be an adequate solution to the wave equation even at boundaries between materials showing strong velocity gradients.

Rays are defined as the normals to a wave front (loci of points that undergo the same motion at a given instant time), pointing in the direction of propagation.

6.5.1. Ray geometry and the raypath equation

The direction cosines associated with a ray normal to a three-dimensional wave front $W(\mathbf{x})$, travelling an arc length s in a time t , are given by dx_1/ds , dx_2/ds , dx_3/ds and must satisfy

$$\left(\frac{dx_1}{ds}\right)^2 + \left(\frac{dx_2}{ds}\right)^2 + \left(\frac{dx_3}{ds}\right)^2 = 1 \quad (6.42)$$

Because the gradient of a function is oriented normal to it we get a physical connection between s and $W(\mathbf{x})$ by stating: $\nabla W(\mathbf{x}) \propto s$ and thus (6.42) can be rewritten as

$$\left(a \frac{\partial W(\mathbf{x})}{\partial x_1}\right)^2 + \left(a \frac{\partial W(\mathbf{x})}{\partial x_2}\right)^2 + \left(a \frac{\partial W(\mathbf{x})}{\partial x_3}\right)^2 = 1 \quad (6.43)$$

If a , as a constant of proportionality, is set to $a = c(\mathbf{x})/c_0$, (6.43) is the eikonal equation

$$\left(\frac{\partial W(\mathbf{x})}{\partial x_1}\right)^2 + \left(\frac{\partial W(\mathbf{x})}{\partial x_2}\right)^2 + \left(\frac{\partial W(\mathbf{x})}{\partial x_3}\right)^2 = \frac{c_0^2}{c(\mathbf{x})^2} \quad (6.44)$$

which relates rays to the seismic velocity distribution and will “ (...) approximate the wave equation well if the fractional change in velocity gradient over one seismic wavelength is small compared to the velocity.” (Lay et al. 1995: 72)

For rays, as a portion of a seismic wavefield, very simple equations are obtained from the eikonal.

The *raypath equation* (6.45) is a generalized form of the *normal* equations obtained through the combination of eq. (6.42) and eq. (6.43):

$$\begin{aligned} \frac{d}{ds} \left(n \frac{dx_i}{ds} \right) &= \frac{\partial n}{\partial x_i} \\ \frac{d}{ds} \left(\frac{1}{c(\mathbf{x})} \frac{d\mathbf{x}}{ds} \right) &= \nabla \left(\frac{1}{c(\mathbf{x})} \right) \end{aligned} \quad (6.45)$$

When following a ray through a material that changes velocity only in one direction (e.g. x_3), (6.45) reduces to

$$n \frac{dx_1}{ds} = c_1 = \text{const}$$

$$n \frac{dx_2}{ds} = c_2 = \text{const}$$

$$\frac{d}{ds} \left(n \frac{dx_3}{ds} \right) = \left(\frac{dn}{dx_3} \right) \quad . \quad (6.46)$$

“The ratio of c_1 and c_2 confines the raypath to a plane that is normal to the x_1x_2 plane. (In other words, the projection of the ray into the x_1x_2 plane is a straight line.)” (Lay et al. 1995: 74)

Choosing this plane to coincide with the x_1x_3 plane, (6.46) reduces to

$$n \left(\frac{dx_1}{ds} \right) = \text{const}$$

$$\frac{d}{ds} \left(n \frac{dx_3}{ds} \right) = \left(\frac{dn}{dx_3} \right) \quad . \quad (6.47)$$

The direction cosine of the ray at a given point is given by

$$l_1 = \frac{dx_1}{ds} = \sin i$$

$$l_3 = \frac{dx_3}{ds} = \cos i \quad . \quad (6.48)$$

and thus

$$\begin{aligned} n \frac{dx_1}{ds} &= \frac{c_0}{c} \sin i = \text{const} \\ \Rightarrow \frac{\sin i}{c} &= \text{const} = p \end{aligned} \quad (6.49)$$

Depending on the orientation of the travel path, the constant p (called *ray parameter* or *horizontal slowness*) varies from 0 (vertical) to $1/c$ (horizontal). The *angle of incidence* i , gives the inclination of a ray measured from the vertical (direction x_3) at any given depth or any point along the travel path. For a given reference point and takeoff angle, the ray parameter p is constant for the entire travel path of the ray. Equation (6.49) is also known as Snell's law. (Lay et al. 1995: 74-75)

6.5.1.1. The travel time equation: the where and the when

As mentioned before, at any point along the travel path we have

$$\begin{aligned}\sin i &= \frac{dx_1}{ds} = cp \\ \cos i &= \frac{dx_3}{ds} = \sqrt{1 - \sin^2 i} = \sqrt{1 - c^2 p^2} \\ \Rightarrow dx_1 &= ds \sin i = \frac{dx_3}{\cos i} cp = \frac{cp}{\sqrt{1 - c^2 p^2}} dx_3\end{aligned}\tag{6.50}$$

For a surface source and receiver, integrating equation (6.50) over the depth will give the distance $X(p)$, at which a ray with ray parameter p will emerge:

$$X(p) = 2 \int_0^z \frac{cp}{\sqrt{1 - c^2 p^2}} dx_3\tag{6.51}$$

z is the maximum depth of penetration and a factor 2 comes from the symmetry of the upgoing and downgoing portions of the raypath. In this case, it is obviously enough to know the angle at which the ray leaves the source, in order to calculate *where* it will arrive. For a general 3-dimensional case, the azimuth of the raypath relative to the source has to be taken into account as well.

The corresponding travel time along the raypath to the distance defined by (6.51) is obtained similarly:

$$T = 2 \int_0^z \frac{dx_3}{c^2 \sqrt{1/c^2 - p^2}}\tag{6.52}$$

Noting the similarity between (6.51) and (6.52) and introducing some shorthand like $\gamma = 1/c$ we can relate the two, resulting in a separable expression for the travel time equation

$$T = pX + 2 \int_0^z \sqrt{\gamma^2 - p^2} dx_3\tag{6.53}$$

where the vertical travel time depends only on the *vertical slowness* $\eta = (\gamma^2 - p^2)^{1/2}$ and the horizontal travel time only on the *horizontal slowness* p , also known as *ray parameter* which is itself equal to the change in travel time with distance:

$$\frac{dT}{dX} = p \quad (6.54)$$

6.5.2. Travel times in a layered earth

Having a velocity structure that represents a layer over a half space with seismic velocities $\alpha_2 > \alpha_1$, three primary travel paths exist between the source and the receiver: (1) the direct arrival, (2) a reflected arrival and (3) a head wave.

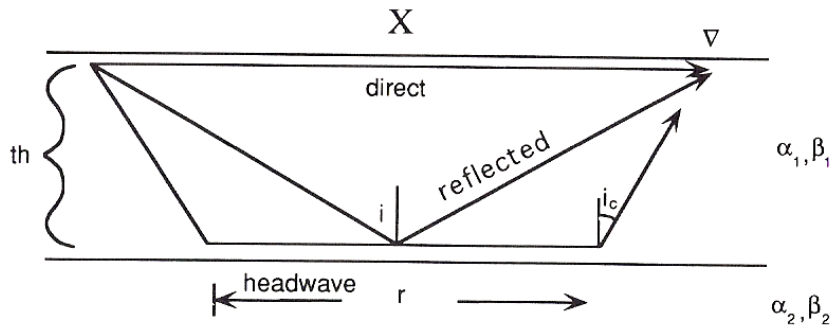


Figure 6.6 the three principal rays in a velocity structure that is a layer of half space

(Source: Lay et al. 1995: 81)

6.5.2.1. Apparent velocity and horizontal slowness

Because of geometric reasons, the wave front of a reflected ray will travel along the surface at a higher velocity than the actual seismic velocity of the layer, and therefore it is called *apparent velocity* α_a .

$$\alpha_a = \frac{x}{\delta t} = \frac{d}{\sin i} \frac{1}{\delta t} = \frac{\alpha_1}{\sin i} = \frac{1}{p} \quad (6.55)$$

For a ray with a vertical incidence on the free surface, p would be zero and α_a infinite. Once again this equation shows where the name *horizontal slowness* for the *ray parameter* p comes from.

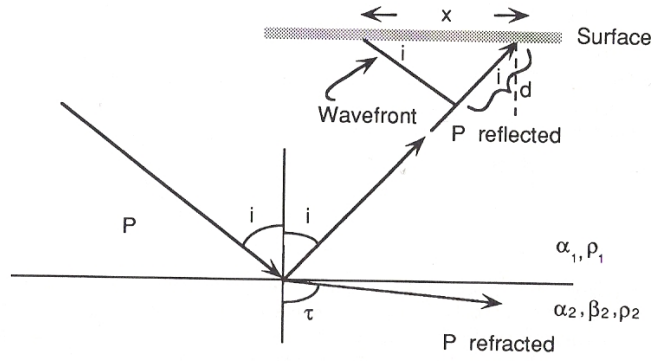


Figure 6.7 P wave hitting a boundary between contrasting materials

(Source: Lay et al. 1995: 80)

6.5.2.2. Travel time equation for a layered earth

Finding travel time equations for rays along the 3 different types of primary travel paths and combining them will lead to the very useful form of the layered structure equivalent to (6.53),

$$T = Xp + 2 \text{ th } \eta_1 \quad (6.56)$$

where $\eta_1 = (1 - p^2 \alpha_1^2)^{1/2} / \alpha_1$. (Lay et al. 1995: 82)

6.5.2.3. The crossover distance

Since the head wave travels with a faster apparent velocity than the direct wave, it becomes the first arrival after a so called *crossover distance* X_c . At X_c the travel times of the direct arrival and the head wave are the same:

$$\begin{aligned} T_{\text{direct}} &= T_{\text{head}} \\ \Rightarrow X_c &= 2 \text{ th } \sqrt{\frac{\alpha_2 + \alpha_1}{\alpha_2 - \alpha_1}} \end{aligned} \quad (6.57)$$

(Lay et al. 1995: 82-83)

6.5.2.4. Apparent velocities for dipping layers

In the presence of a dipping layer, head waves have different apparent velocities depending on whether the rays are travelling *updip* or *downdip*, since the wave fronts are incident on the surface at different angles (fig. 6.8).

$$\frac{1}{v_u} = \frac{\sin(i_c - \theta)}{v_1}$$

$$\frac{1}{v_d} = \frac{\sin(i_c + \theta)}{v_1}$$
(6.58)

i_c ... critical angle, θ ... dip of layer

(Lay et al. 1995: 87-88)

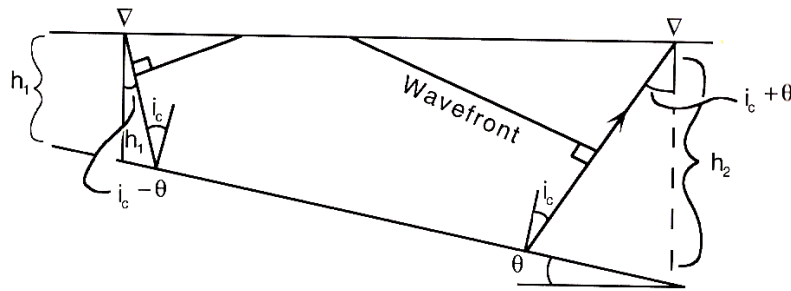


Figure 6.8 raypath geometry for head waves along a dipping interface

(Source: Lay et al. 1995: 88)

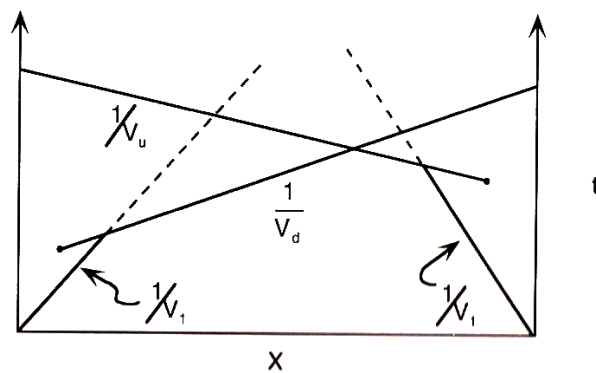


Figure 6.9 travel time curves for a dipping structure (time increasing to the right for downdip and time increasing to the left for updip direction)

(Source: Lay et al. 1995: 88)

Bibliography

Arens, T.; Hettlich, F.; Karpfinger, C.; Kockelkorn, U.; Lichtenegger, K.; Stachel, H. (2008): Mathematik. Heidelberg: Spektrum Akademischer Verlag

Bell, F. G. (1998): Environmental Geology. Principles and Practice. New Jersey: Wiley

Brückl, E.; Brunner, F. K.; Kraus, K. (2006a): Kinematics of a deep-seated landslide derived from photogrammetric, GPS and geophysical data. IN G.B. Crosta, R.J. Shlemon, C.H. Juang, C. Carranza-Torres (Eds.), Engineering Geology 88, (pp. 149 - 159). Amsterdam: Elsevier

Brückl, E.; Brückl, J. (2006b): Geophysical models of the Lesachriegel and the Gradenbach deep-seated mass-movements (Schober range, Austria). IN G.B. Crosta, R.J. Shlemon, C.H. Juang, C. Carranza-Torres (Eds.), Engineering Geology 83. p. 254-272. Amsterdam: Elsevier

Brückl, E.; Parotidis, M. (2005): Prediction of slope instabilities due to deep-seated gravitational creep. IN F. Guzzetti, B.D. Malamud, S. Tinti, U. Ulbrich (Eds.), Natural Hazards and Earth System Sciences. Vol. 5. pp. 155-172. Göttingen: Copernicus GmbH

Lang, C.; Pucker, N. (2005): Mathematische Methoden in der Physik. 2nd edition. München: Spektrum Akademischer Verlag

Lay, T.; Wallace, T. (1995): Modern global seismology, San Diego: Academic Press, Inc.

Marui, H. (1988): Food and Agriculture Organization of the United Nations watershed management field manual: landslide prevention measures, Volume 4, Rome.

Mertl, S.; Brückl, E. (2008): Hazard Estimation of Deep Seated Mass Movements by

Microseismic Monitoring. ISDR20 Final Report 2004 - 2008. Institute of Geodesy and Geophysics, Vienna University of Technology. Vienna: September 2008

Scherbaum, F. (2007): Of Poles and Zeros, Fundamentals of Digital Seismology, Revised 2nd Edition, Netherlands: Springer

Smith, S. W. (2003): Digital Signal Processing. A practical guide for engineers and scientists. Burlington: Newnes as imprint of Elsevier Science

Schurr, B. (2007): Digitale Signalanalyse. Lecture notes. WS 2007.

Vaseghi, S. (2008): Advanced digital signal processing and noise reduction. 4th edition. UK: John Wiley & Sons Ltd

Weidner, S.; Moser, M.; Lang, E. (2011): Geotechnische und kinematische Analyse des Talzuschubes Gradenbach (Kärnten/Österreich). Jahrbuch der geologischen Bundesanstalt. Band 151, Heft 1+2, p.17-60. Wien: Dezember 2011

Internet sources:

U.S. Geological Survey: Landslides types and processes. Fact Sheet 2004-3072. 2004
<http://pubs.usgs.gov/fs/2004/3072/pdf/fs2004-3072.pdf>
[last downloaded: 2013-02-27]

Bäk, R.: Deep creeping mass-movements. 2 case studies. Carinthia, Austria. 2002
http://www.ktn.gv.at/9923_DE-Geologie_und_Bodenschutz-GB_DEEP_CREEPING_MASS_MOVEMENTS_.pdf
[last downloaded: 2013-02-27]

REF TEK: Broadband seismic recorders.
<http://www.reftek.com/products/seismic-recorders-130-01.htm>
[last downloaded: 2013-02-27]

List of figures

- Figure 1.1** abbreviated version of Varnes' classification of slope movements (1978) (<http://pubs.usgs.gov/fs/2004/3072/pdf/fs2004-3072.pdf> [2013-02-27]), p.4
- Figure 2.1** tectonic map and location of the Gradenbach deep-seated mass-movement (Brückl et al. 2006b: 255), p.6
- Figure 2.2** topography of the Gradenbach landslide area: all GPS stations of the monitoring network are shown; for scale estimation: the horizontal distance between Ref 2 and A is 2600 m (Brückl et al. 2006 a: 150), p.7
- Figure 2.3** geologic-geotechnical map of the Gradenbach landslide (Weidner et al. 2011: 22), p.8
- Figure 2.4** devastated village of Putschall (1968) (Weidner et al. 2011: 20), p.9
- Figure 2.5** topography and location of seismic lines and boreholes (Brückl et al. 2006b: 256), p.10
- Figure 2.6** seismic cross sections of Gradenbach landslide. (above: GB78_01, below: GB78_02) (http://www.ktn.gv.at/9923_DE-Geologie_und_Bodenschutz-GB_DEEP_CREEPING_MASS_MOVEMENTS_.pdf [2013-02-27]), p.11
- Figure 2.7** P-wave velocity models of the creeping rock mass and the stable rock base (B) GB98_01, (C) GB98_02 (Brückl et al. 2006b: 259), p.12
- Figure 2.8** Gradenbach monitoring network, (Mertl et al. 2008: 3), p.13
- Figure 3.1** recording unit Reftek 130-01 (<http://www.reftek.com/products/seismic-recorders-130-01.htm> [27-02-2013]), p.15
- Figure 3.2** polar plot of "visible" near earthquakes; the radius is the epi-distance in degrees; for data selection purposes a function returns the information needed to find the events in the database when clicking on the individual marker; author: myself, p.18
- Figure 3.3** histogram of "visible" local earthquakes (blue) and near earthquakes

(black) with different magnitudes; "local" means an epicentral distance smaller than 150 km; the x-axis indicates the direction of the occurring events relatively to the GB monitoring stations; the circles mark the directions where to look for clusters of events in the polar plot (fig. 3.2), p.19

- Figure 3.4** visible (a) and not visible (b) event filtered with a 4th order butterworth bandpass (lower cutoff: 2Hz, upper cutoff: 12 Hz), p.20
- Figure 3.5** spatial distribution of final dataset, p.22
- Figure 3.6** temporal distribution of final dataset, p.22
- Figure 3.7** recording the displacement spectrum of an idealized earthquake source, (Scherbaum 2007: 140), p.23
- Figure 3.8** recovering the source spectrum by inverse filtering, (Scherbaum 2007: 141), p.23
- Figure 3.9** transfer function of a 1 Hz seismometer with a damping of 0.707, p.25
- Figure 3.10** transfer function of a 4.5 Hz seismometer with a damping of 0.707, p.25
- Figure 3.11** inverse transfer function of a 1 Hz seismometer with a damping of 0.707, p.26
- Figure 3.12** inverse transfer function of a 4.5 Hz seismometer with a damping of 0.707, p.26
- Figure 3.13** transfer function of a 2-pole butterworth highpass with a cutoff frequency of 0.8 Hz, p.27
- Figure 3.14** "analog" filter consisting of the inverse transfer function of a 1 Hz seismometer and a highpass with a cutoff frequency of 0.8 Hz., p.27
- Figure 3.15** "analog" filter consisting of the inverse transfer function of a 4.5 Hz seismometer and a highpass with a cutoff frequency of 0.8 Hz, p.28
- Figure 3.16** bilinear transformed digital filter consisting of the inverse transfer function of a 1 Hz seismometer and a highpass with a cutoff frequency of 0.8 Hz, p.28
- Figure 3.17** bilinear transformed digital filter consisting of the inverse transfer function of a 4.5 Hz seismometer and a highpass with a cutoff frequency of 0.8 Hz, p.29
- Figure 3.18** exported data (window length: 12 s, start: 2 s before first break), p.29
- Figure 3.19** ProMAX data import, p.30

- Figure 3.20** "inverse filtered" data with bandpass, p.31
- Figure 3.21** spectral analysis of "inverse filtered" data with bandpass, p.32
- Figure 3.22** an example for a correlation window with 800 ms in length, p.33
- Figure 3.23** time picking of maxima of received auto and cross correlations, p. 34
- Figure 3.24** generic continental crustal structures and schematic travel time curves where Pg is a wave in the upper crust, P* is a wave in the lower crust or along the Conrad discontinuity and Pn is a head wave, refracted below the Mohorovičić discontinuity; the 150 km mark the crossover distance, (Lay et al. 1995: 254), p.36
- Figure 3.25** central European Moho with lines into direction Poland (25°) and Italy (210°) to estimate the dip of the Moho around the investigation side, p.37
- Figure 3.26** sketchy geometrical considerations for a correction of the epicentral distances regarding the direction of propagation of the incident wave front, p.39
- Figure 3.27** horizontal travel time differences (Poland), p.40
- Figure 3.28** horizontal travel time differences (Italy), p.41
- Figure 3.29** horizontal travel time differences (Austria), p.42
- Figure 3.30** plot of travel time residuals over the stations' heights using an average velocity for the solid rock of 4500 m/s, p.43
- Figure 3.31** plot of travel time residuals over the stations' heights using an average velocity for the solid rock of 5500 m/s, p.44
-
- Figure 4.1** final results for "Poland" showing reduced mean travel time differences; the shaded contour plot in the background indicates the thickness of the moving mass, p.45
- Figure 4.2** final results for "Italy" showing reduced mean travel time differences; the shaded contour plot in the background indicates the thickness of the moving mass, p.45
- Figure 4.3** final results for "Austria" showing reduced mean travel time differences; the shaded contour plot in the background indicates the thickness of the moving mass, p.46
- Figure 4.4** final results showing reduced mean travel time differences of all the events put together; the shaded contour plot in the background indicates

- the thickness of the moving mass, p.46
- Figure 4.5** final results plotted over the thickness of the moving rock mass, p.47
- Figure 6.1** RC circuit (Scherbaum 2007: 12), p. 56
- Figure 6.2** frequency response function and the eigenvector/eigenvalue concept (Scherbaum 2007: 20), p.59
- Figure 6.3** mapping of the complex s-plane onto the complex z-plane; the imaginary axis is mapped onto the unit circle, the right half s-plane onto the outside of the unit circle and the left half s-plane onto the interior of the unit circle in the z-plane (Scherbaum 2007: 157), p.62
- Figure 6.4** vertical pendulum seismometer (Scherbaum 2007: 49), p.63
- Figure 6.5** the cross correlation function has its maximum at lag D which corresponds to the time delay in demand (Vaseghi 2008: 84), p.67
- Figure 6.6** the three principal rays in a velocity structure that is a layer of half space, (Lay et al. 1995: 81), p.72
- Figure 6.7** P wave hitting a boundary between contrasting materials (Lay et al. 1995: 80), p.73
- Figure 6.8** raypath geometry for head waves along a dipping interface (Lay et al. 1995: 88), p.74
- Figure 6.9** travel time curves for a dipping structure (time increasing to the right for downdip and time increasing to the left for updip direction) (Lay et al. 1995: 88), p.74

Curriculum vitae

Personal information

Surname, First names Domenig, Angela Isabella
e-mail angela.domenig@gmx.at
Nationality AUT
Date of birth 03. 03. 1987

Education

2005 - 2013

Studies of geophysics at the University of Vienna, Austria

1993 - 2005

School education in Hermagor, Austria

Mother tongue German

Other languages

	Understanding	Speaking	Writing
English	very good	very good	very good
Italian	good	good	good
Icelandic	good	good	adequate

Norwegian - basics

Turkish - basics

Experiences abroad

August 2003 - February 2004

Exchange student at Menntaskólinn á Akureyri, Iceland

Study-related work experiences

April 2011

Employer AIT - Austrian Institute of Technology
Employment level Freelancer
Tasks Assistance in vibration measurements

		August 2010
	Employer	Geological Survey of Austria, Vienna, Austria
	Employment level	Intern
	Tasks	Geoelectrical field measurements, maintenance of measuring cables
		July 2008 - September 2008
	Employer	Geophysik – International Geophysical Services (IGS) GmbH, Leipzig, Germany
	Employment level	Intern
	Tasks	Geoelectrical and gravimetric field measurements, maintenance, repair and overhaul of measuring instruments, assistance in interpreting seismic data and geological structures in the subsurface
		2005 - 2008
	Employer	Steinhauser Erschütterungsschutz, Vienna, Austria
	Employment level	Freelancer
	Tasks	Assistance in seismic measurements for acquiring vibration immissions or for vibration prognosis from tunnel borings and rail traffic
Interests, skills and competences		
	Music	2006 - 2010
		Member of the university orchestra of Vienna, Austria
		1992 - 2005
		Violin lessons at the music school Hermagor, Austria
		Participation in several music competitions
		Graduation from music school with distinction in 2005
		1999 – 2004
		Drums and percussion lessons at the music school Hermagor, Austria
		Participation in several music competitions
	Sports	Playing soccer, kickboxing, cycling, swimming, snowboarding, running, trekking
	Further interests	Foreign countries, languages and cultures, movies, books, animals
	Licences	Driving licence (B - car), blasting licence